A thermo-frictional tyre model including the effect of flash temperature

The version of record of this manuscript has been published and is available in *Vehicle System Dynamics*, 2018, http://www.tandfonline.com **, DOI: 10.1080/00423114.2018.1484147**

Georgios Mavros*, Loughborough University

A new tyre model is developed that can predict the influence of both macroscopic and local flash temperature on tyre force generation. The model comprises two heat-transfer solvers. A macroscopic solver calculates the 3D temperature distribution across the tread and sidewall at a resolution of a few millimetres. A separate flash-temperature solver calculates the local hot-spot temperature distribution at the macro-asperity tyre-road contact interface at a resolution of micrometres. The two heat-transfer solvers are coupled with a structural model for the calculation of tyre forces and the sliding speed distribution along the contact patch. The sliding speed distribution feeds into the flash temperature model and the local coefficient of friction is found as a function of sliding speed, flash temperature, normal pressure, road roughness and the complex modulus of rubber. The proposed tyre model is the first to include the effect of a changing macroscopic temperature distribution on the build-up of the local flash temperature and to account for road-tread conduction at the macro-asperity contact interface. The model is applicable for identifying the friction envelope and optimum temperature range for tyres on roads with a known roughness. This is important in motorsport where knowledge of grip offers a competitive advantage.

Keywords: tyre model; heat-transfer; friction; temperature; rubber; road surface roughness

Introduction

The experiments carried out by Grosch [1] were the first to demonstrate the strong relationship between the frequency response of rubber and its friction against a hard substrate. Grosch found that the variation of friction with temperature follows exactly that of the rubber's stress-strain FRF (frequency response function) with temperature. The latter is quantified by the WLF (Williams, Landel and Ferry) equation [2], which predicts a horizontal shift of the FRF to the right of the logarithmic frequency scale, as the temperature of the rubber increases. Grosch distinguished two different components in rubber friction, namely *adhesion* and *deformation*. The former involves molecular interaction and manifests on smooth surfaces and at low speeds, while the latter is related to high-speed sliding on rough surfaces. Both mechanisms were found to be dependent on the bulk viscoelastic properties of rubber.

In line with Grosch's findings, Persson [3] developed a theory of rubber friction and contact mechanics that can predict the coefficient of friction as a function of the power spectral density of a randomly rough surface, the complex modulus of rubber, its temperature, normal pressure and sliding speed. The theory presented in [3] is valid for rubber with uniform temperature and assumes negligible frictional heating due to sliding.

Grosch's experimental findings and Persson's rubber contact and friction theory are important in understanding the friction of tyres on racing tracks, as discussed by Sharp et al [4]. Grosch's experiments were partly replicated in [4] using Persson's friction equation, albeit using rubber material properties from the literature, to cater for the lack of knowledge of the properties of the actual material used by Grosch. It is argued in [4] that Persson's theory fails to correlate with measurements at low sliding speeds where the adhesion peak is expected, since the theory disregards adhesion altogether as an insignificant contribution. Persson, on the other hand, [3] argues that, based on surface free energy, adhesion manifests only at wavelengths $\lambda<0.1$ μm and he then claims that interaction at such small length-scales is prohibited due to surface contamination.

*Email: g.mavros@lboro.ac.uk

Persson updated his rubber friction theory to account for the flash temperature effect [5], showing that friction can be significantly reduced because of the formation of brief localised hot patches at the interface between macroscopic asperities and the rubber. The proposed analytical calculation of flash temperature-affected friction assumes an adiabatic boundary with the road and a constant background temperature for the rubber. The flash temperature model was used within a transient tyre model in [6]. Due to the significant computational cost of the analytical solution, a phenomenological friction law was implemented that agreed well with the complete flash model but is also restricted to a constant bulk temperature. This is an important limitation in motorsport and in normal driving conditions where the bulk temperature of the tyre is expected to vary significantly due to repetitive loading of the tyre.

To date, Persson's tyre model [6] seems to be the only one incorporating analytical calculation of friction but does not account for variations of a tyre's bulk temperature. Other models [7-12] focus on macroscopic temperature calculation and use empirically or semi-empirically derived laws for the dependency of friction on temperature and/or speed.

In the following sections a new thermo-frictional tyre model is presented, incorporating an alternative approach for modelling the flash temperature. The suggested method alleviates the assumptions of an adiabatic boundary with the road and a constant/uniform macroscopic temperature distribution within the tyre.

Macroscopic heat transfer

Rubber is a material of low thermal conductivity [13], so significant temperature gradients are expected within the tread. Especially during transient manoeuvres such as emergency braking, it is expected that high temperatures will develop locally, at the outer layers of the tread or even restricted to a small part of the circumference, in the case of wheel lock. To account for such gradients, a fully three-dimensional treatment of heat transfer is adopted. The main features of the heat-transfer model are summarized below:

- Three-dimensional heat transfer model of the tyre including tread and sidewalls
- Heat generation due to frictional interaction at the contact
- Heat generation due to bulk deformation of the tyre
- Conductive heat transfer between tread and road
- Convective and radiative heat transfer from the inside carcass surfaces to the air inside the tyre
- Convective and radiative heat transfer to the environment
- Variable temperature boundary at the inside of the rim (to account for rim heating, for example)

A graphical representation of the modes of heat transfer is provided in fig. 1.

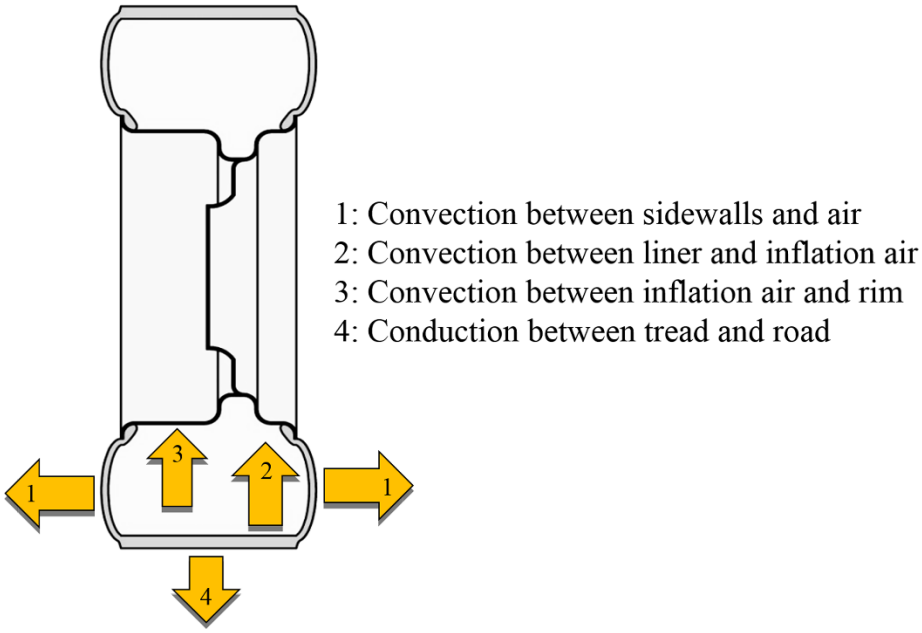

Figure 1. Modes of heat transfer

Referring to the cylindrical frame of reference shown in fig. 2 the equation of heat transfer for the tyre tread and sidewall is written in cylindrical coordinates as follows [14]:

$$\rho c_p \frac{\partial T}{\partial t} = \lambda_r \frac{\partial^2 T}{\partial r^2} + \lambda_r \frac{1}{r}\frac{\partial T}{\partial r} + \lambda_\varphi \frac{1}{r^2}\frac{\partial^2 T}{\partial \varphi^2} + \lambda_z \frac{\partial^2 T}{\partial z^2} + \Phi \quad (1)$$

The corresponding equation for the road in rectangular coordinates reads [14]:

$$\rho c_p \frac{\partial T}{\partial t} = \lambda_x \frac{\partial^2 T}{\partial x^2} + \lambda_y \frac{\partial^2 T}{\partial y^2} + \lambda_z \frac{\partial^2 T}{\partial z^2} \quad (2)$$

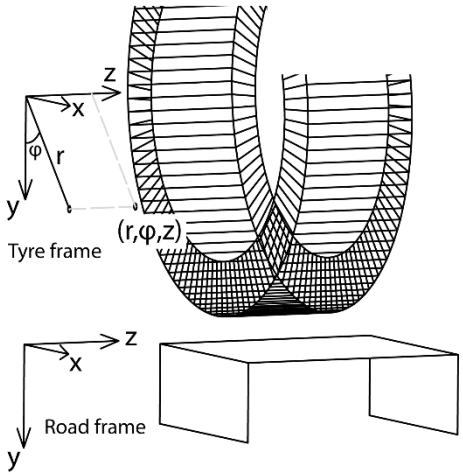

Figure 2. Tyre and road frames of reference

In the above equations ρ is the material density $[kgm^{-3}]$, c_p is the specific heat $[m^2K^{-1}s^{-2}]$, $\lambda_{r,\varphi,z}$ are the thermal conductivities in the respective directions $[W(mK)^{-1}]$, T is the temperature in $[^oC]$ and Φ is the heating power per unit volume $[Wm^{-3}]$.

Note that, in line with the theory of friction, only the tyre equation (1) includes a heating term, as it is rubber hysteresis that is solely responsible for frictional heating. This is true irrespective of whether one considers adhesion or not, since it is shown that the adhesive interaction also depends on the bulk parameters of rubber [1] and adhesive friction is – like deformation friction – a result of periodic loading of rubber (albeit at molecular level).

Equations (1) and (2) are discretised and solved using a central difference scheme for the spatial temperature distribution and a forward difference for the temporal evolution of temperature.

The tyre interacts with the surrounding environment through convection, conduction and radiation (although the latter effect is negligible). Here, convective and radiative boundaries are converted into conductive boundaries by augmenting the actual conductive mesh with the addition of an external auxiliary layer of conductive nodes. The temperature of these nodes is determined so that the conductive heat flux between them and the actual surface nodes of the conductive mesh is equal to the corresponding convective/radiative heat flux. Thus, the convective/radiative boundary is transformed into a temperature boundary. Equivalent results can be obtained by considering the energy balance for the surface nodes [14]. However, the augmented mesh approach is preferred here as it leads to a more efficient formulation of the problem, especially applicable to a rotating/contacting structure such as the tyre.

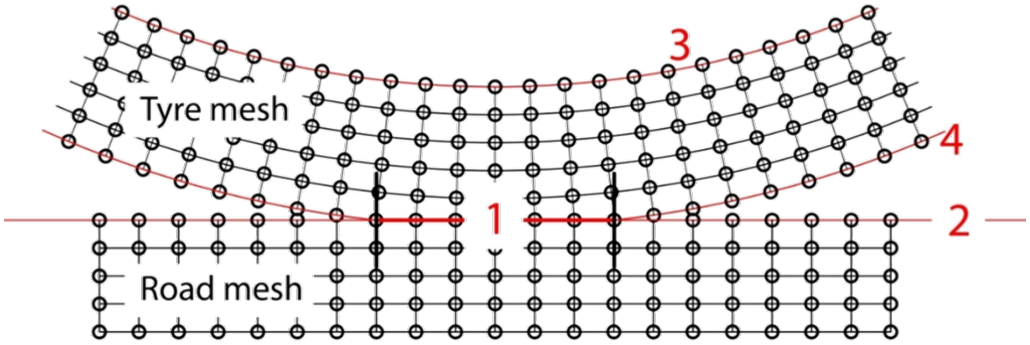

Figure 3. Auxiliary Layers. Layer 1 is the common auxiliary layer between tyre and road, layer 2 is the auxiliary layer between the road and open air, layer 3 is the auxiliary layer on the inside of the tyre carcass and layer 4 is the one between the external tread surface and the open air.

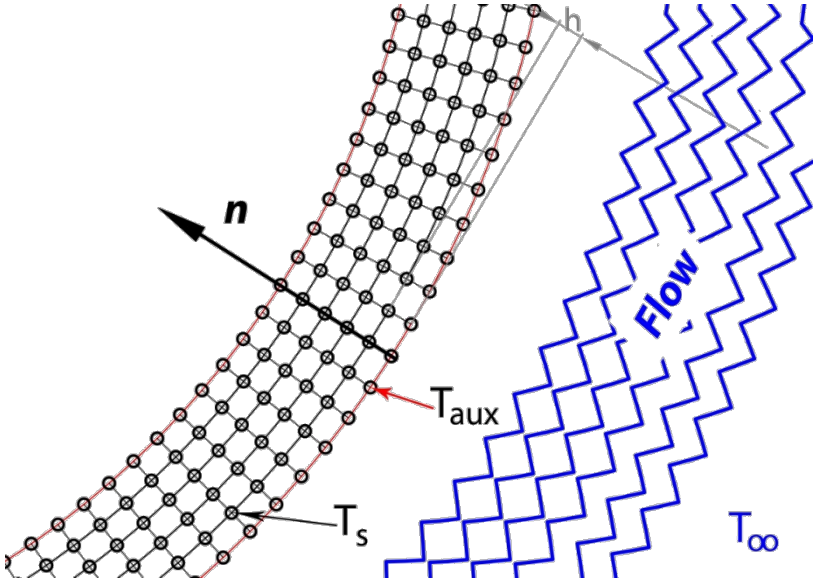

Figure 4. Boundary interaction with outside air

The derivation of the temperature of an auxiliary layer node is presented for the outer tyre surface. Fig. 3 shows a view of the tyre and the road interacting with each-other and with the surrounding open air. In fig. 3 the virtual auxiliary layers are numbered from 1-4. The external auxiliary layer of nodes (layer 4 in fig. 3) runs along the circumference of the tyre. This virtual layer is assumed to lie at a radial distance, h, equal to the radial discretisation of the actual tyre mesh. The interaction between a tread surface node and the open air is considered first. Referring to fig. 4, the following equation provides the heat flux from the tyre surface with temperature, T_s, to the air with temperature, T_∞:

$$q_s = h_{CONV}(T_\infty - T_s) - \varepsilon\sigma_{SB}T_s^4 \quad (3)$$

The first right-hand-side term in equation (3) is related to convection with h_{CONV} representing the convection coefficient in $[WK^{-1}m^{-2}]$. The second term is due to radiation with ε representing the emissivity of rubber and σ_{SB} the Stefan-Boltzmann constant $[WK^{-4}m^{-2}]$. Note that no interaction via radiation is assumed with potential surrounding bodies, such as the wheel arches or the road. The above convective/radiative heat flux must equal the conductive heat flux on the surface:

$$q_s = -\lambda_r \frac{\partial T}{\partial \mathbf{n}_T} \approx -\lambda_r \frac{T_s - T_{aux}}{h} \quad (4)$$

Combining equations (3) and (4) yields:

$$T_{aux} = \frac{h_{CONV}(T_\infty - T_s)h}{\lambda_r} - \frac{h\varepsilon\sigma_{SB}T_s^4}{\lambda_r} + T_s \quad (5)$$

The temperature of all auxiliary nodes that are in interaction with the air is updated at every time step using equation (5).

The tyre-road common auxiliary layer requires a different treatment. To calculate the temperature of a node of the common auxiliary layer, it is assumed that the distance between the tyre and the road is infinitesimally small. Because the thickness of the layer approaches zero, there is no heat storage and the heat fluxes towards the tyre and the road are equal. With this assumption, the following equation is derived:

$$q_s = -\left(\lambda_r \frac{\partial T}{\partial \mathbf{n}_T}\right)_{Tyre} = -\left(-\lambda_y \frac{\partial T}{\partial \mathbf{n}_T}\right)_{Road} \therefore -\lambda_r \frac{T_{St} - T_{aux}}{h} = \lambda_y \frac{T_{Sr} - T_{aux}}{v} \quad (6)$$

In the above equation, v is the size of the road mesh in the downwards (y) direction (see fig. 2). If it is further assumed that the mesh dimensions in the radial tyre direction (h) and the downwards road direction (v) are equal, the following expression is found for the temperature of a node of the common auxiliary layer:

$$T_{aux} = \frac{\lambda_y T_{Sr} + \lambda_r T_{St}}{\lambda_y + \lambda_r} \quad (7)$$

The above result represents a weighted average of the tyre and road surface temperatures with the weighting factors being the corresponding thermal conductivities. It follows that if the thermal conductivities are equal, the temperature of a node of the common auxiliary layer is the arithmetic mean of the temperature of the adjacent road and tyre nodes. The above treatment allows computationally efficient switching between the two auxiliary layers (air and road) depending on the position of the tyre. Simulations have shown that, especially when the tyre is moving at moderate speeds, the temperature of the road can be assumed constant (see Appendix A). Under such conditions solution of eq. (2) is unnecessary and eq. (7) can be used with a constant road temperature T_{Sr}.

The internal auxiliary layer interacts with the inflation air inside the tyre cavity. Thus, the air temperature increases and the convective heat flux gradually reduces. To account for this, the change in air temperature is calculated as follows:

$$Q_S = m_{air} C_v \frac{dT}{dt} \quad (8)$$

Where T is the air temperature, m_{air} is the mass of the air $[kg]$, C_v is the air's specific heat capacity under constant volume and Q_S represents the total heating power $[W]$ from the tyre liner nodes, as well as due to convective interaction between the air and the rim.

The increase in inflation air temperature results in an increase in pressure via the ideal gas equation $PV = nRT$, where P is the pressure $[Pa]$, V is the inflation volume $[m^3]$, n is the number of gas moles, $R = 8.314$ is the ideal gas constant $[JK^{-1}mol^{-1}]$ and T is the temperature in $[K]$. For simplicity, the inflation volume is considered constant, although the model includes provision for *inflation stiffness*, defined as the rate of change of volume with gauge pressure $[m^5N^{-1}]$. The latter parameter requires identification via experiments or a high-fidelity finite element model of the tyre and is out of the scope of the present work. More so, since in the experiments carried out for model parameterisation/validation (see next section), the inflation pressure was kept constant. Thus, the heating of the inflation air only affects tyre behaviour via changes in convection, not in pressure.

Parameterisation and validation of the macroscopic heat-transfer model

A modular approach has been adopted so that the macroscopic heating model can be parameterised and validated in isolation from the other components (flash-temperature, structural) using measured tyre forces, temperatures and slips. The macroscopic heat-transfer model can then be used in conjunction with the flash temperature model presented later herein, or in combination with other, widely used, tyre models. Indeed, the model has been successfully linked with the Magic Formula model [15]. To create a stand-alone functional heat-transfer module, a method is required to distribute heating power throughout the tyre body.

To contain computational cost, a simple phenomenological law is used for the distribution of heating power. The total power resulting from tyre force generation due to slip inputs (not including rolling resistance) is equal to:

$$W_{slip} = W_X + W_Y = |F_x \sigma_x V_r| + \left|F_y \sigma_y V_r\right| \quad (9)$$

In the above equation, σ indicates the "theoretical" slip quantities and V_r is the linear speed of rolling, as defined in [16]. The two terms in eq. (9) are further split into tread surface contribution and hysteretic bulk contribution terms. The former corresponds to surface power due to the tread sliding against the road, while the latter is due to bulk deformation of the tread/belt. This is indicated by the following equation:

$$W_{X,Y} = \left|F_{x,y} \sigma_{x,y} V_r\right| = W_{X,Ysurface} + W_{X,Ybulk} \quad (10)$$

It is expected from basic brush-model theory [16], that, as the vertical load on a tyre increases, the percentage of sliding along the tread reduces and so does the surface term in eq. (10). It is also expected that, as the slip increases, the surface term in eq. (10) increases in the expense of the bulk term. These trends are captured by the following phenomenological law that provides the surface power term, as a function of the total power term:

$$W_{X,surface} = e^{-\left(\frac{F_Z}{F_{x,ref}}\right)} \left(1 - e^{-\frac{|\sigma|}{B_x}}\right) W_X \quad (11)$$

$$W_{Y,surface} = e^{-\left(\frac{F_Z}{F_{y,ref}}\right)}\left(1 - e^{-\frac{|\sigma|}{B_y}}\right)W_Y \quad (12)$$

In the above equations F_Z is the vertical load on the tyre, $F_{x,ref}$ and $F_{y,ref}$ are constant reference loads for the longitudinal and lateral case respectively, and $B_{x,y}$ are non-dimensional parameters that regulate the rate at which surface power increases with slip. The slip magnitude $|\sigma|$ is defined as follows:

$$|\sigma| = \sqrt{\sigma_x^2 + \sigma_y^2} \quad (13)$$

Power due to sliding at the contact is assigned only at the outer layer of nodes of the tread. The remaining heating power is distributed evenly in the tread at a depth, H_T, from the surface. In line with reference [17], approx. 85% of rolling resistance power is uniformly distributed in the belt/tread with 15% left for the sidewall. The necessary rolling resistance coefficient is assumed a quadratic function of the linear speed of rolling so that:

$$C_{RR} = rr_a V_r + rr_b V_r^2 \quad (14)$$

Where C_{RR} is the rolling resistance coefficient defined here as the ratio between rolling resistance force and vertical load both expressed in $[N]$, V_r is the linear speed of rolling and $rr_{a,b}$ are experimentally identified coefficients. This simple rolling resistance law captures the expected quadratic behaviour of the rolling resistance coefficient as a function of rolling speed, see for example [18], albeit without including a constant term. While the constant term is necessary to deal with the full range of speeds in the context of studying rolling resistance, it is omitted here for economy of parameters and so that the model does not predict a finite rolling resistance force at zero speed, which would cause the wheel to move spontaneously. The speed range during testing for parameterisation and validation of the model was limited between approx. 10 and 30 $[ms^{-1}]$ and the adopted law proved sufficient to predict sensible rolling resistance coefficients of 0.003 and 0.01 at the two speed extremes, respectively. A generally weak dependency of C_{RR} on vertical load is observed [19], while a strong dependency is expected on temperature and inflation pressure [18], [19]. The inclusion of such effects lies outside the scope of the present work and it should be noted that all testing was carried out with a constant tyre pressure – automatically regulated to account for heating of inflation air.

The lateral distribution (along z-axis, see fig. 2) of heating power due to camber angle is given by the following linear law:

$$W(z,\gamma) = W\left(1 - \frac{\gamma}{\gamma_{ref}}\right) + 2W\frac{\gamma}{\gamma_{ref}}\bar{z} \quad (15)$$

Where W is the total power, γ is the camber angle in degrees, γ_{ref} is an identifiable reference camber angle and $\bar{z}$ is the normalised lateral position along the tread, starting from one edge of the tread. The reference camber angle dictates how skewed the power distribution becomes due to transversely uneven contact pressure. The physical significance of γ_{ref} is that, when $\gamma = \gamma_{ref}$, the heating power reduces to zero at one edge of the tread, while increasing to double the calculated value at the other end. For heat distribution calculation purposes, the actual camber angle is capped to a maximum of γ_{ref}, so that negative heating does not occur.

To calculate external cooling effects due to convection, a single average convection coefficient is used which is assumed a linear function of speed, as follows:

$$h_{CONV} = h_a + h_b V_r \quad (16)$$

Where h_{CONV} is the convection coefficient in $[WK^{-1}m^{-2}]$, V_r is the linear speed of rolling $[ms^{-1}]$ and $h_{a,b}$ are experimentally identifiable constants with units $[WK^{-1}m^{-2}]$ and $[WK^{-1}m^{-3}s]$.

The primary heat-transfer model parameters such as the specific heat and conductivities in different directions (see eq. (1)), together with the secondary empirical parameters included in eq. (11), (12), (14), (15) and (16) were all identified via tyre testing at the Calspan tyre testing facility in Buffalo, US. The parameterisation approach employed here aims to be efficient and economical, without increasing the experimental overhead. As such, it uses traditional flat-track tyre testing to estimate all parameters. For greater accuracy, estimation of parameters such as thermal conductivities, heat capacities, convection coefficients and the rolling resistance coefficient can be carried out separately using laboratory techniques [13], [19], [20]. In the spirit of efficiency and economy of parameters, the heat conductivities and specific heat capacities of the materials are considered constant. It is shown through measurements on reinforced rubber composites [13], that the diffusivity (defined as $\lambda/\rho c_p$) can vary up to about 15-25% within the temperature range of interest, say from 30°C to 140°C. Such variations have been implemented in other thermal tyre models, see for example [21]. The assumption of temperature-independent heat transfer parameters results in estimating mean values, but this approach has been found adequate in most cases, as discussed shortly.

Several tyres were subjected to a long sequence of varying lateral/longitudinal slip and camber inputs at varying vertical loads and road speeds. Tyre forces, internal (carcass liner) and external tread temperatures, as well as the track surface temperature were acquired during the experiments. The heat-transfer model was supplied with the experimentally measured slip inputs, loads and environment (air and track) temperatures and non-linear least-squares optimisation was used to identify the set of parameters that provided the best correlation between measured and simulated temperatures. Specifically, the Matlab function “lsqnonlin” was employed to minimise a penalty function that effectively consists of the sum of the squared differences between measured and estimated tread surface temperatures and half the sum of the squared differences between measured and estimated carcass liner temperatures. The default trust-region-reflective algorithm [22] has been shown to converge rapidly when sensible initial estimates together with upper and lower bounds are provided. Typically, convergence is achieved in approx. 20 iterations and the process of identifying all parameters takes between 40-60 mins.

For validation, the model was subjected to a different input sequence and the RMS (root-mean-square) error between measured and simulated temperatures was calculated. Typical RMS errors at the identification stage were found to be around 5-7%, while at validation stage these were slightly increased at 7-8%. Fig. 5 shows the correlation between measured/simulated tread surface temperatures at validation stage, while fig. 6 shows the corresponding carcass liner temperature correlation. Both results correspond to an all-season tyre with its dimensions included in Appendix B. In fig. 6 there appears to be an occasional hesitation of the simulated liner temperature to follow the measured one. This is evident around 200 s, 2000 s and 3000 s into the simulation. It must be stressed that the input sequence was particularly testing, with load variations in excess of 1000% up to peak loads higher than 10 [KN] taking place within a few seconds, in combination with severe combined slip, camber and speed variations. Such extreme conditions represent a worst-case scenario and reveal the influence of several factors including the simplifications in rolling resistance representation, the fact that the internal convective heat transfer coefficient is assumed independent of speed, lack of experimental knowledge of the rim temperature, lack of experimental knowledge of initial inflation air temperature and highly non-linear effects that cause large scale deformations and complex hysteretic loss distributions that cannot be fully captured by simple phenomenological laws such as those presented in eq. (10)-(16). Still, with all simplifications, agreement with measurements is good even in such extreme conditions and parameterisation is exceptionally efficient.

The final set of parameters is presented in table B.1 in appendix B. In all cases the identified parameters were found to be very close to nominal/measured parameters from the literature (see for example the heat-transfer parameters measured in [13] and [20]).

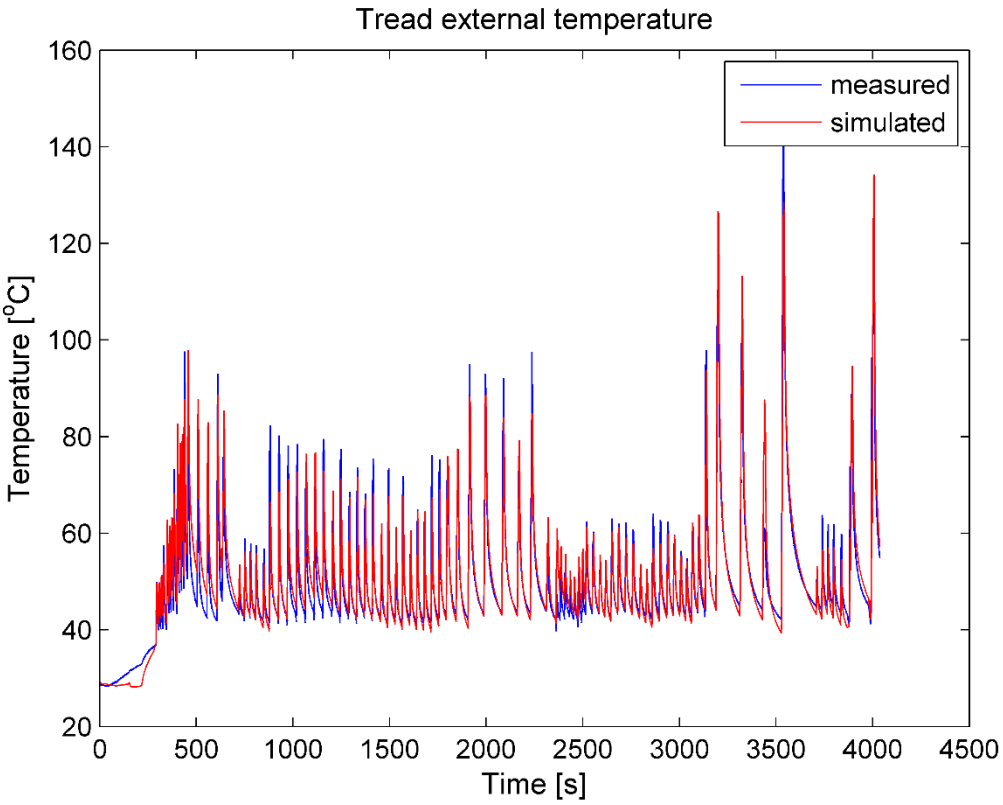

Figure 5. Comparison between measured/simulated tread temperatures. The temperature RMS error is 6.69%

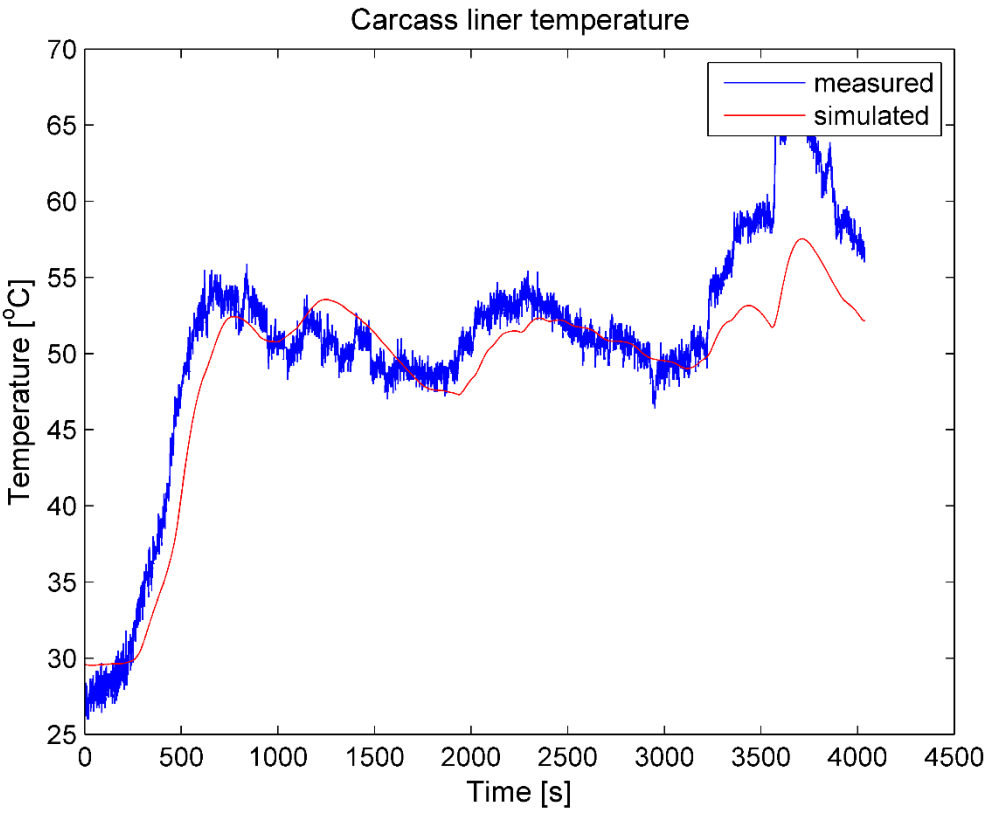

Figure 6. Comparison between measured/simulated internal liner temperatures

Note in table B.1 (Appendix B) that the radial discretisation of the tread is identified via optimisation. This is because all surface power (see eq. 10) is supplied to the external tread layer, so the volume of this layer influences peak temperatures. Similarly, the tread depth, H_T, throughout which the bulk sliding power is distributed, is also identified via optimisation.

Flash temperature model

The predicted temperature distribution from the macroscopic heat transfer model is too coarse to account for the flash temperature effect. To appreciate the effect of flash temperature one needs to consider the rubber-road contact in detail. It is established that most rough surfaces consist of small asperities lying on larger asperities, which, in turn lie on larger asperities [23]. Therefore, roughness exists at several length scales, or wavelengths, λ, from $\lambda{\sim}10^{-6}\ m$ up to $\lambda{\sim}10^{-2}\ m$ for a typical road. The asperity amplitude, h, at each different length-scale, λ, may vary in general but it is found that most road surfaces follow the structure of self-affine fractals [24], [3], [5]. This implies that, if a magnification ζ is applied in the $x,\ y$ directions of a road surface, the observed asperity pattern will be repeated precisely if a magnification ζ^H is applied in the z direction (height of asperities), where parameter H is the Hurst exponent. Such surfaces have a PSD (Power Spectral Density) given by an equation of the type [3]:

$$C(q) = \frac{(h_0/q_0)^2 H}{2\pi}\left(\frac{q}{q_0}\right)^{-2(H+1)} \quad for\ q \geq q_0\ and\ C(q) = \frac{(h_0/q_0)^2 H}{2\pi}\ for\ q < q_0 \quad (17)$$

In the above equation, q is the wavevector, expressed as $q = 2\pi/\lambda$ [m^{-1}], parameter q_0 is the roll-off wavevector below which the power spectral density of the road remains constant and h_0 is the asperity height at q_0. The PSD used throughout this paper is shown in fig. 7.

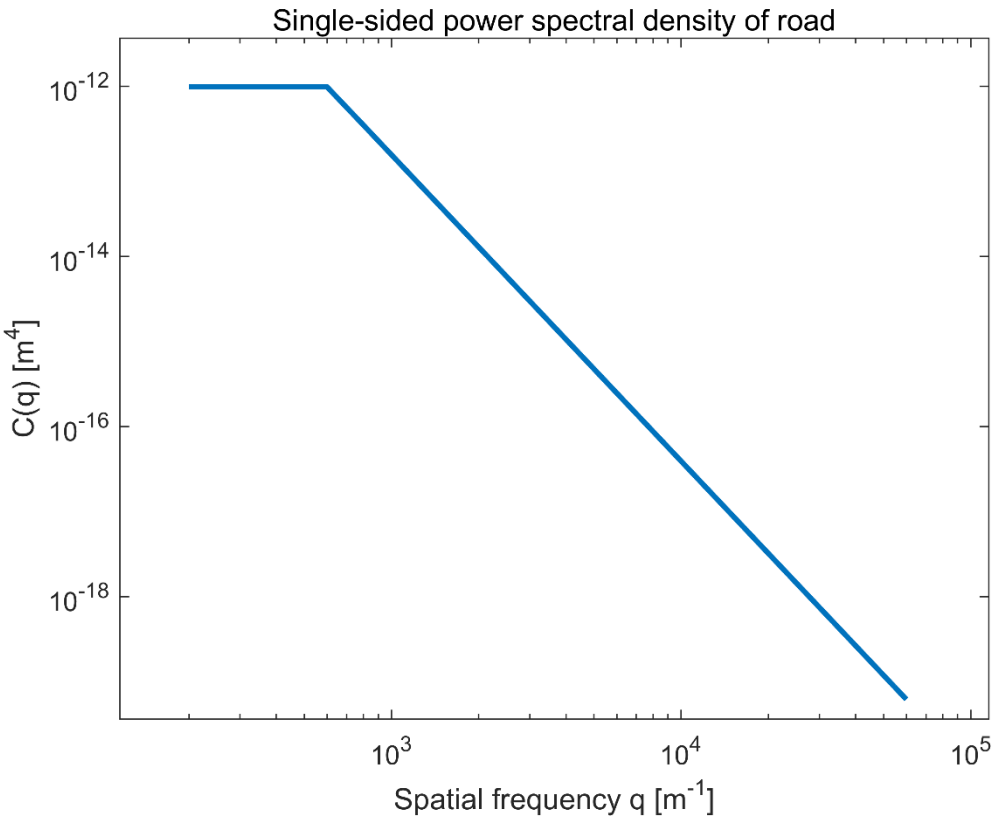

Figure 7. PSD of a fractal-type road with $q_0 = 600\ m^{-1}$, $h_0 = 0.0017\ m$ and $H = 0.8$

The key to understanding flash temperature is considering the contact at wavelengths $q_m \sim \zeta_m q_0, \zeta_m = 2 \dots 5$. At this magnification, the rubber makes apparent contact with the road at sparsely distributed areas of average size of a few millimetres, known as macro-asperity contact areas [5]. All the heating power due to friction is concentrated in these hot-spots which may rapidly develop very high temperatures. Since friction is the result of interaction between rubber and road at different wavelengths, it is expected that the larger wavelengths will heat rubber at a greater depth. At such depths, the effect of heating due to interaction at smaller wavelengths is negligible. On the contrary, at shallower depths the heating effect of all asperities that interact at larger depths is accumulated. Therefore, it is expected that a different temperature T_q is relevant when interacting with different wavevectors, q. Persson has accounted for these effects in his two analytical solutions of flash temperature [5] which provide the temperature vector T_q for both fully developed as well as transient sliding conditions. With knowledge of T_q for every q, the coefficient of friction is given by [5]:

$$\mu = \frac{1}{2}\int_{q_0}^{q_1} dq \cdot q^3 C(q) P(q) \int_0^{2\pi} d\varphi cos\varphi Im \frac{E(qUcos\varphi, T_q)}{(1-\nu^2)\sigma_o} \quad (18)$$

$$P(q) = \frac{2}{\pi}\int_0^{\infty} dx \frac{sin(x)}{x} \exp\left(-x^2 G(q)\right) \quad (19)$$

$$G(q) = \frac{1}{8}\int_{q_0}^{q} dq \cdot q^3 C(q) \int_0^{2\pi} d\varphi \left|\frac{E(qUcos\varphi, T_q)}{(1-\nu^2)\sigma_o}\right|^2 \quad (20)$$

In the above equations $P(q)$ is the contact ratio, i.e. the ratio between the apparent contact area at length $\lambda = 2\pi/q$ and the apparent contact area at $\lambda_0 = 2\pi/q_0$. E is the complex modulus of rubber, v is Poisson's ratio, σ_0 is the nominal contact pressure and U is the sliding speed. The dependency of the rubber's complex modulus on temperature is given by the Williams-Landel-Ferry equation [2]. The upper integration limit, q_1, is the cut-off wavevector associated with the smaller wavelengths at

which the rubber interacts with the substrate. It is typically limited due to contamination and the formation of a thin 'dead' layer on the surface of rubber [5]. This is a thin layer where rubber has degraded due to excessive mechanical and thermal stressing and can be assumed to have a negligible contribution to rubber friction. For further information on the short-distance cut-off the reader is referred to [5] and the references therein.

In the steady-state case, the calculation of T_q is an iterative process, while in the transient case a significant number of nested integrals require calculation. In both cases the process is computationally very intensive. More importantly, both analytical solutions assume a constant bulk rubber temperature and adiabatic boundary between the rubber and the road surface. The constant temperature assumption poses great limitations since, the local heating of the rubber near the contact patch as predicted by the macroscopic heat transfer model, cannot be included in the calculation.

To overcome this limitation a circular macro-contact area with radius R is considered and the flash temperature problem is reformulated in cylindrical coordinates as follows:

$$\rho c_p \frac{\partial T}{\partial t} = \lambda_r \frac{\partial^2 T}{\partial r^2} + \lambda_r \frac{1}{r}\frac{\partial T}{\partial r} + \lambda_\varphi \frac{1}{r^2}\frac{\partial^2 T}{\partial \varphi^2} + \lambda_z \frac{\partial^2 T}{\partial z^2}$$

$$-Ucos\varphi \frac{\partial T}{\partial r} + \frac{U}{r} sin\varphi \frac{\partial T}{\partial \varphi} + \dot{Q}H(R-r) \quad (21)$$

In the above equation ρ is the material density $[kgm^{-3}]$, c_p is the specific heat $[m^2K^{-1}s^{-2}]$, $\lambda_{r,\varphi,z}$ are the thermal conductivities $[W(mK)^{-1}]$, T is the temperature $[^oC]$, U is the sliding speed $[ms^{-1}]$ and $\dot{Q}$ is the heating power per unit volume $[Wm^{-3}]$. The z-coordinate extends depth-wise into the tread, r extends radially and φ is the angular coordinate. H represents the Heaviside function.

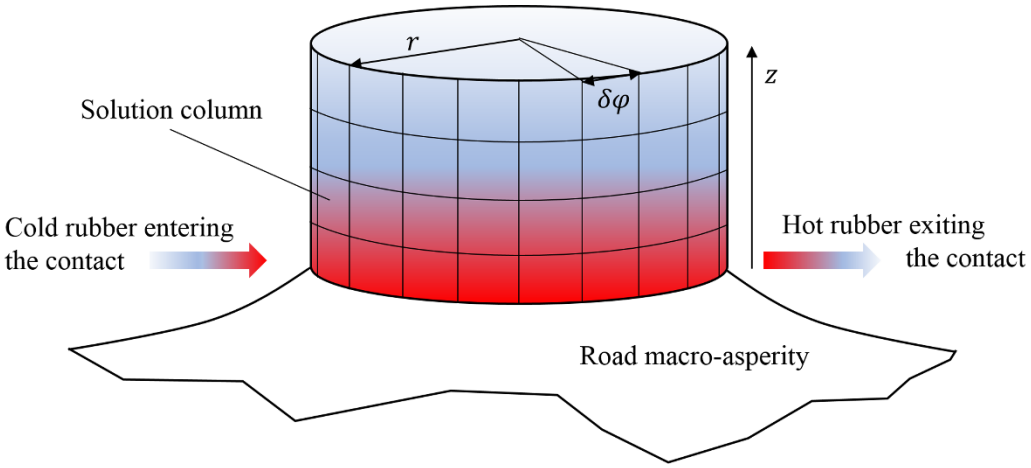

Figure 8. The flash-temperature solution column remains stationary with respect to the road asperity with cold rubber entering and hot rubber exiting the boundaries at a rate dictated by the sliding speed.

Equation (21) refers to a cylinder extending vertically above the circular macro-asperity contact area with boundaries that are stationary with respect to the road, as shown in fig. 8. As the rubber slides over the contacting macro-asperity, material moves within the cylinder volume and a temperature gradient develops as indicated by the velocity-related terms in eq. (21). The Heaviside function ensures that frictional power is restricted radially within the boundaries of the cylinder. The friction power per volume is a function of depth, z, and is given by the equation [5]:

$$\dot{Q}(z,t) = U\int_{q_0}^{q_1} dq \cdot e^{-2qz} q^4 C(q) \frac{P(q)}{P(q_m)} \int_0^{2\pi} d\varphi cos\varphi Im \frac{E\left(qUcos\varphi, T_q\right)}{(1-\nu^2)} \quad (22)$$

Where $P(q_m)$ is the contact ratio at wavelength q_m where the sparse macro-contact areas are observed.

The radius, R, of the assumed circular macro-asperity contact is given by [5]:

$$Rq_m = a + b\left(\frac{A(\zeta_m)}{A_0}\right)^c, a = 0.526, b = 3.636, c = 0.729 \quad (23)$$

In eq. (23) $A(\zeta_m)$ is the apparent contact area at magnification ζ_m, or, alternatively, wavelength $q_m = \zeta_m q_0$ and A_0 is the contact area at wavelength q_0. Their ratio is typically between 0.25-0.3 [5].

Equation (21) is discretised and solved using a central difference scheme for the spatial temperature distribution and a forward difference scheme for the temporal evolution of temperature. Equation (22) represents a weighted exponential distribution of heating power with the maximum at the surface and rapid reduction toward the inside of the tread. The required depth of the cylinder depends on the road's spectral density, the sliding speed and the rubber's complex modulus, but in most cases heating reduces to insignificant levels at depths $d \sim 1 \ldots 5\times10^{-3}\ m$. The cylinder boundaries are augmented using auxiliary layers, like in the macroscopic model. The temperature of the top auxiliary surface of the solution volume (cylinder) is set equal to the local temperature of the tread as predicted by the macroscopic heat-transfer model. The rear half of the cylinder's circumferential auxiliary layer experiences new material entering the solution volume and the corresponding temperature is also set equal to the local temperature of the tread as predicted by the macroscopic heat-transfer model. The nodes of the front half of the cylinder's circumferential auxiliary layer are given the temperature of the nodes at the actual boundary of the cylinder at the previous timestep, i.e. an adiabatic boundary is assumed.

Having calculated the temperature distribution throughout the cylinder, the vector T_q is calculated as follows:

$$T_q(t) = \frac{\int_0^R rdr \int_0^{2\pi} d\varphi \int_0^\infty dz T(r,\varphi,z,t)\exp(-2qz)}{\int_0^R rdr \int_0^{2\pi} d\varphi \int_0^\infty dz \exp(-2qz)} \quad (24)$$

Eq. (24) is a modified version of the corresponding equation in [5], to account for transverse temperature variation.

The flash temperature model is verified in isolation using a cured, carbon-filled SBR (styrene-butadiene rubber) rubber with 40 phr carbon black [25]. The complex modulus of the 40 phr carbon black SBR rubber is reproduced from [25] and shown in fig. 9 at a reference temperature of -48°C.

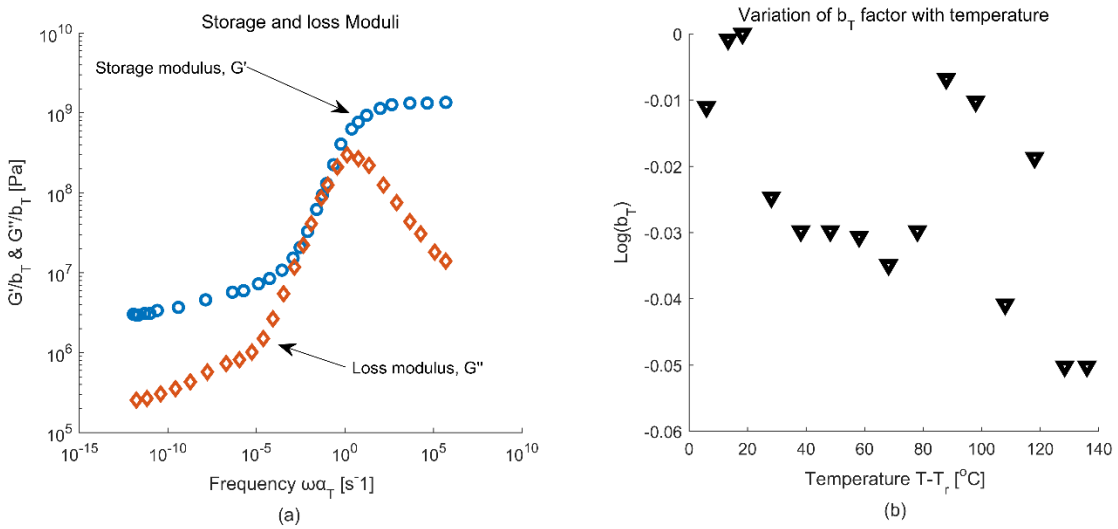

Figure 9. Storage and loss moduli master curves of 40 phr carbon-black SBR at -48°C (a) and variation of amplitude factor with temperature (b) for the same rubber, reproduced from [25]. Note that the temperature is the difference between actual and reference temperature (-48°C).

Filled rubbers show a temperature dependent complex modulus according to the equation:

$$E(\omega, T) = b_T E(\omega a_T, T_r) \quad (25)$$

The horizontal shift as a function of temperature for the selected rubber is given by the WLF equation [25]:

$$log a_T = \frac{-C_1(T-T_r)}{C_2+(T-T_r)}, C_1 = 15.1, C_2 = 46.1, T_r = -48^o C \quad (26)$$

The amplitude factor, b_T, for the selected rubber is reproduced from [25] and is also shown in fig. 9. In this case b_T shows a weak and largely random dependency on the difference between actual and reference temperatures but is still included here for completeness of material characterisation. The reader is referred to reference [25] for examples of rubbers with different carbon-black concentrations and varying levels of b_T.

The friction between the 40 phr carbon-black SBR rubber and a rough road surface defined by eq. (18) is shown in fig. 10, for three different temperatures. The results in the figure correspond to a uniform temperature throughout the rubber, so the effect of flash temperature is neglected. The predicted friction curves are in close agreement with curves presented in [3] for similar rubbers and road surfaces. The results are also in line with the measurements in [1], however it has not been possible to experimentally validate the predictions, as these are based on a nominal PSD and rubber properties found in the literature [25].

The parameters used in the flash-temperature model are given in table C.1 in appendix C, while the road surface is the same as that used in fig. 10 ($q_0 = 600\ [m^{-1}]$, $h_0 = 0.0017\ [m]$, $H = 0.8$ and maximum magnification $\zeta_{max} = 100$). As seen in fig. 10, friction drops significantly at higher temperatures. To show a meaningful variation of the coefficient of friction, the initial temperature of the rubber block is set to 0°C and the sliding speed is 2 ms^{-1}. The flash temperature model was first ran assuming no conduction (as per Persson's assumption [5]) and then including conduction with the road. The latter case was modelled considering an identical solution cylinder extending depth-wise into the road surface with an auxiliary layer at the interface between rubber/road. To simulate conduction, the temperature at the auxiliary layer was calculated as per eq. (7). The temperature at the circumferential and bottom boundaries of the cylindrical volume within the road were assumed at a

constant temperature equal to the initial rubber/road temperature, i.e. 0°C. The velocity and heating power terms were omitted from eq. (21).

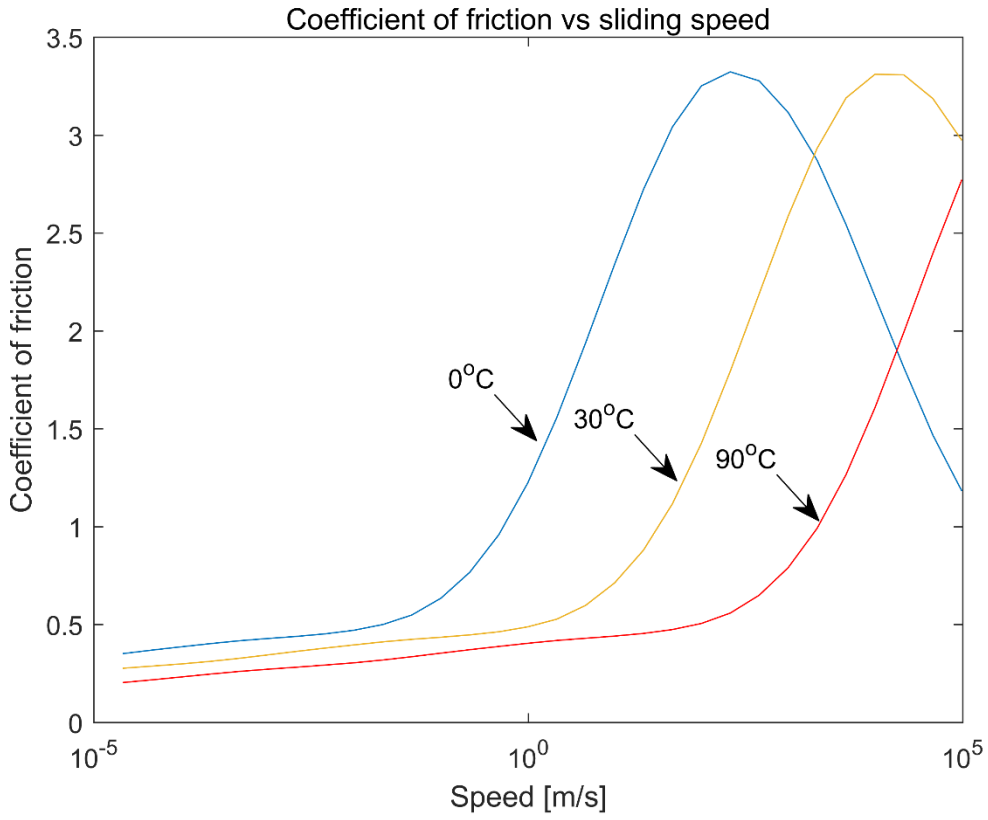

Figure 10. Coefficient of friction of 40 phr carbon-black SBR rubber slid against a substrate with $q_0 = 600\ m^{-1}$, $h_0 = 0.0017\ m$, $H = 0.8$ and maximum magnification $\zeta_{max} = 100$. The nominal contact pressure is $\sigma_0 = 2e5\ Pa$ and the Poisson ratio is $\nu = 0.5$.

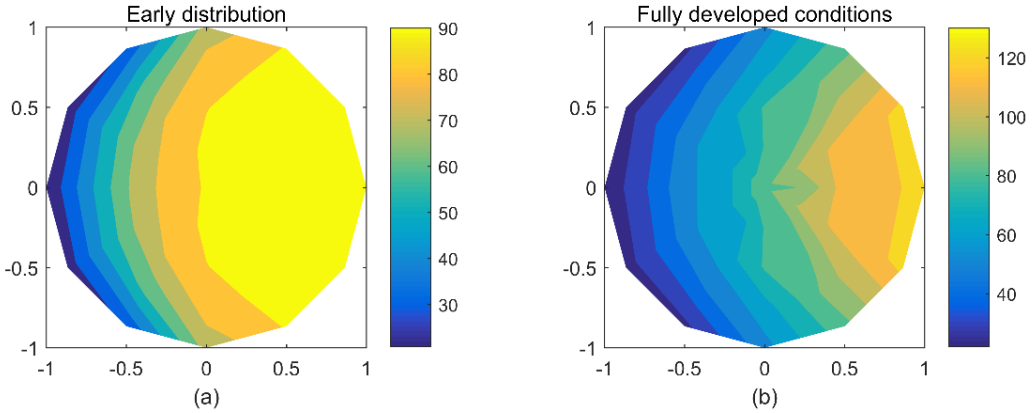

Figure 11. Rubber surface temperature distribution at the macro-asperity contact when (a) the rubber has slid a length of 1 mm and (b) at fully developed conditions, having slid 4 mm. The sliding speed is 2 ms^{-1} and conduction with the road is neglected.

Fig. 11 shows the temperature distribution at the rubber surface at an early stage and when conditions have fully developed. The rubber slides from left to right and conduction with the road is neglected. The left-to-right temperature gradient is due to cool rubber entering the solution volume from the left. Fig. 12 shows the corresponding fully-developed conditions when conduction with the road is

included. The rubber surface is significantly cooler than in fig. 11 (b) while at the same time the road has heated significantly. The time evolution of the mean temperature at the surface layer of the rubber and the corresponding friction are shown in fig. 13 with and without conduction with the road. The result without road conduction agrees well with Persson's prediction [5] both in terms of temperature and friction, albeit Persson has shown the evolution of T_{qmax}, which represents a weighted average of the temperature along the z-axis of the solution cylinder. The friction here drops quicker to lower values (see fig. 10) and this explains the somewhat reduced maximum contact temperature in fig. 13. Still, the temperature evolution shows an exponential increase like in [5] with a peak which is slightly more pronounced than in [5], presumably due to showing the actual surface temperature as opposed to a weighted average. The rubber surface temperature with road conduction takes longer to reach steady-state and the peak has disappeared due to a significant energy flow toward the road. It is very likely that eq. (7) over-predicts conduction with the road and that in fact the flash temperature lies somewhere between the two curves in fig. 13 (a). Surface contamination and the percentage of contact at different magnifications will determine conduction with the road and this is an area that requires further investigation.

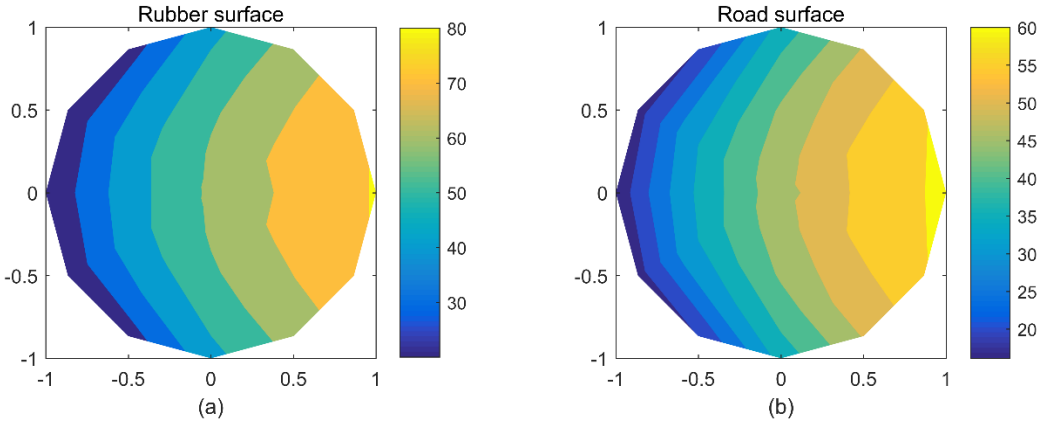

Figure 12. Temperature distribution at the rubber surface (a) and road surface (b), assuming conduction between the rubber and the road. The snapshot is at 2 ms, when the rubber has slid by 4 mm.

It must be noted that the behaviour shown in fig. 13 is common, but not universal. Whether friction decays or improves with temperature depends on the combination of surface roughness, rubber material properties and operating conditions. For example, in [5] friction is found to generally reduce with temperature, but other researchers [12] have implemented a friction law derived in [26] to generate tyre force curves that show an increase in friction with temperature. It must be noted that the friction law in [26] includes a semi-empirical approximation of friction due to adhesion, which is also dependent on the viscoelastic properties of rubber. This inclusion adds an adhesion hump at very low sliding speeds, that is responsible for the increase in friction with temperature.

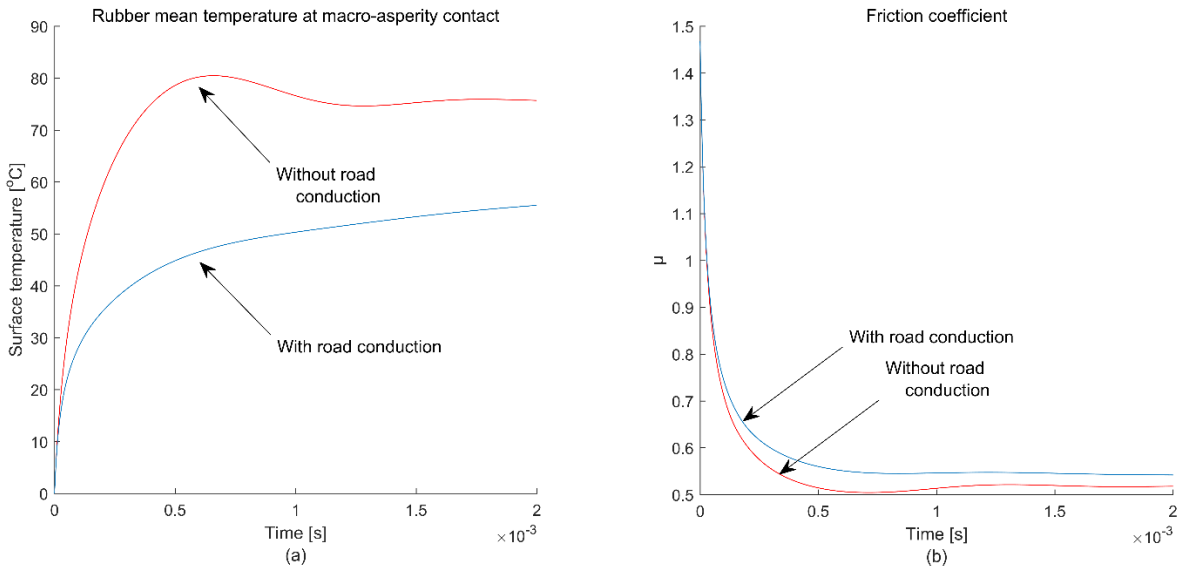

Figure 13. Time evolution of the rubber's surface temperature (a) and the overall coefficient of friction including the effect of flash temperature (b).

Structural model

Calculation of the flash temperature along the contact patch of the tyre requires knowledge of the normal pressure and sliding speed distributions along the contact patch. A flexible ring on elastic foundation model is employed for the lateral and tangential deformations of the belt. To reduce the computational cost of the model, radial belt deformations are not included and the normal pressure distribution is assumed parabolic so that:

$$f_z(x) = \frac{3F_z}{4\mathrm{a}}\left(1 - \left(\frac{x}{\mathrm{a}}\right)^2\right) \quad (27)$$

Where f_z is the load distribution $[Nm^{-1}]$, a is the half length of the contact patch $[m]$ so that the contact is completely symmetric extending $(-\mathrm{a}, \mathrm{a})$ from the longitudinal centre of the contact, F_z is the total normal load $[N]$ and x is the position along the contact patch. The half-length of the contact patch is given by: $\mathrm{a} = \sqrt{2RF_z/C_z}$, where R is the radius of the tyre $[m]$ and C_z is the vertical tyre stiffness $[Nm^{-1}]$.

With the above simplification, the belt model does not require coupling with a radial bed of springs to represent the tread, nor is there a need for a contact-search algorithm, as is the case for example in [27], where the normal load is calculated from the coupled radial/tangential belt deformations and tread deflection. The assumptions governing the derivation of the equations of motion are summarised below:

- Radial modes that include flexing of the belt are not considered since a parabolic pressure distribution is assumed
- Only two orthogonal radial modes with the belt represented as a rigid ring are included, since these have a significant influence on the local longitudinal slip distribution
- Lateral and tangential deflections are not coupled with each-other
- Non-linear couplings such as gyroscopic and Coriolis effects are neglected

It must be noted that this simplified approach serves merely as a mechanical "carrier" model that provides a means of calculating the contact speed distribution and associated friction force but is not

designed to deal with the common non-linearities and three-dimensional couplings observed in tyre dynamics. Such three-dimensional non-linear effects are simulated successfully by state-of-the-art structural tyre models such as those presented in [8] and [12].

Fig. 14 shows a schematic of the structural part of the tyre model. Note that the frame of reference used here is not the same as that used for the heat-transfer model. The reader is referred to the book by Soedel [28] and the theses of Gong [29] and Zegelaar [30] for the treatment of the tyre as a flexible ring with or without elastic foundation.

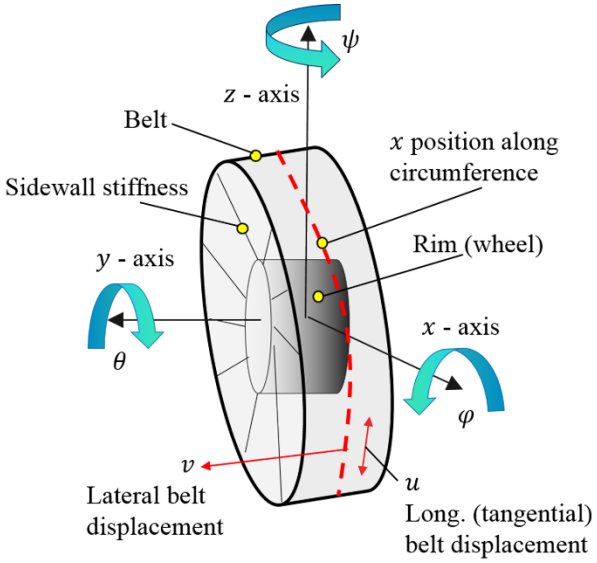

Figure 14. Structural model of the tyre

In the remainder of this section, the out-of-plane and in-plane equations of the tyre-rim system are presented. The solution of these equations via modal expansion and the mass-normalisation of the respective eigenfunctions is detailed in Appendix D.

The equations of lateral motion of the tyre belt-rim combination read:

$$\rho A\frac{\partial^2 v}{\partial t^2}+EI\frac{\partial^4 v}{\partial x^4}-P_o bR\frac{\partial^2 v}{\partial x^2}+k_y v-k_y y_{\omega_0}-k_y\varphi_{\omega_1}Rcos\left(\frac{x}{R}\right)$$

$$-k_y\psi_{\omega_1}Rcos\left(\frac{x}{R}-\frac{\pi}{2}\right)=f_y(x,t)\ (28)$$

$$m_w\ddot{y}_{\omega_0}+k_y 2\pi R y_{\omega_0}-k_y\int_0^{2\pi R}v dx=F_{yw}(t)\ (29)$$

$$Ixx_w\ddot{\varphi}_{\omega_1}+k_y R^2\varphi_{\omega_1}\int_0^{2\pi R}cos^2\left(\frac{x}{R}\right)dx-k_y R\int_0^{2\pi R}cos\left(\frac{x}{R}\right)v dx=M_x(t)\ (30)$$

$$Izz_w\ddot{\psi}_{\omega_1}+k_y R^2\psi_{\omega_1}\int_0^{2\pi R}cos^2\left(\frac{x}{R}-\frac{\pi}{2}\right)dx-k_y R\int_0^{2\pi R}cos\left(\frac{x}{R}-\frac{\pi}{2}\right)v dx=M_z(t)\ (31)$$

In eq. (28)-(31) v is the lateral deflection of the belt $[m]$, x is the linear position along the belt circumference, y is the lateral displacement of the wheel $[m]$, φ is the camber displacement of the wheel $[rad]$, ψ is the yaw displacement of the wheel $[rad]$, ρ is the tyre belt density $[kgm^{-3}]$, A is the cross-sectional area of the belt $[m^2]$, E is Young's modulus $[Nm^{-2}]$, $I=db^3/12$ is the second moment of area $[m^4]$ with d being the depth of the tread and b the width of the tread $[m]$, P_o is the inflation pressure (gauge) $[Nm^{-2}]$, R is the radius of the belt $[m]$, k_y is the effective lateral stiffness of the sidewall per unit length $[Nm^{-2}]$, m_w is the mass of the wheel $[kg]$, Ixx_w, Izz_w are the camber and yaw moments of inertia of the wheel $[kgm^2]$, f_y is the lateral load distribution along the belt

$[Nm^{-1}]$, F_{yw} is the net lateral load on the wheel $[N]$ and $M_{x,z}$ are the roll and yaw moments on the wheel $[Nm]$.

The equations of tangential/rotational motion of the tyre belt-rim combination read:

$$\rho A\frac{\partial^2 u}{\partial t^2} - EA\frac{\partial^2 u}{\partial x^2} + k_x u - k_x R\theta_{\omega_0} = f_x(x,t) \text{ (32)}$$

$$Iyy_w\ddot{\theta}_{\omega_0} + k_x 2\pi R^3\theta_{\omega_0} - k_x R\int_0^{2\pi R} u dx = T_w(t) \text{ (33)}$$

In eq. (32)-(33) u is the tangential deflection of the belt $[m]$, x is the linear position along the belt circumference, θ is the rotational displacement of the wheel $[rad]$, ρ is the tyre belt density $[kgm^{-3}]$, A is the cross-sectional area of the belt $[m^2]$, E is Young's modulus $[Nm^{-2}]$, R is the radius of the belt $[m]$, k_x is the effective longitudinal stiffness of the sidewall per unit length $[Nm^{-2}]$, Iyy_w is the moment of inertia of the wheel about its spin -axis $[kgm^2]$, f_x is the longitudinal load distribution along the belt $[Nm^{-1}]$ and T_w is the net torque on the wheel $[Nm]$.

The last modes considered result from radial displacement of the belt relative to the rim, as described by the equations:

$$2\pi R\rho A\ddot{x}_b + k_r\int_0^{2\pi R} x_b cos^2\left(\frac{x}{R}\right)dx - k_r\int_0^{2\pi R} x_w cos^2\left(\frac{x}{R}\right)dx = F_{bx}(t) \text{ (34)}$$

$$m_w\ddot{x}_w + k_r\int_0^{2\pi R} x_w cos^2\left(\frac{x}{R}\right)dx - k_r\int_0^{2\pi R} x_b cos^2\left(\frac{x}{R}\right)dx = F_{wx}(t) \text{ (35)}$$

$$2\pi R\rho A\ddot{x}'_b + k_r\int_0^{2\pi R} x'_b cos^2\left(\frac{x}{R}-\frac{\pi}{2}\right)dx - k_r\int_0^{2\pi R} x'_w cos^2\left(\frac{x}{R}-\frac{\pi}{2}\right)dx = F'_{bx}(t) \text{ (36)}$$

$$m_w\ddot{x}'_w + k_r\int_0^{2\pi R} x'_w cos^2\left(\frac{x}{R}-\frac{\pi}{2}\right)dx - k_r\int_0^{2\pi R} x'_b cos^2\left(\frac{x}{R}-\frac{\pi}{2}\right)dx = F'_{wx}(t) \text{ (37)}$$

In eq. (34)-(37) x_b and x'_b are two orthogonal displacements of the belt while x_w and x'_w are two orthogonal displacements of the rim. The x symbol has been used in both belt/rim displacements to indicate that they are due to the cyclic application of the longitudinal contact force around the circumference, not due to a vertical and longitudinal force. In this context $F_{bx}(t) = \cos\left(\frac{x(t)}{R}\right)F_{xcontact}(t)$ and $F'_{bx}(t) = \cos\left(\frac{x(t)}{R}-\frac{\pi}{2}\right)F_{xcontact}(t)$ where $x(t)$ is the constantly changing application position of the contact force $F_{xcontact}$ on the circumference. The remaining symbols share the same meaning as in previous equations while k_r is the radial sidewall stiffness per unit length $[Nm^{-2}]$ and F_{wx}, F'_{wx} are the wheel-rim forces $[N]$.

Eq. (34)-(37) are written with respect to degrees of freedom x_b, x_w, x'_b and x'_w, as opposed to using directly the radial eigenfunctions of the belt for $n = 1$, see for example [31]. This approach results in more efficient handling of the purely longitudinal loads at the contact patch. However, calculation of the longitudinal velocity distribution along the contact patch requires the use of the corresponding radial eigenfunctions $x_b cos\left(\frac{x}{R}\right)$, $x'_b cos\left(\frac{x}{R}-\frac{\pi}{2}\right)$ for the calculation of the sliding speed distribution.

The above equations for lateral, tangential/rotational and radial motion are solved by modal expansion and the corresponding eigenfunctions are mass-normalised (see Appendix D). The eigenfunctions are then discretised into eigenvectors and used together with their corresponding eigenvalues, to formulate system matrices that are used in a time-domain solution. This solution provides the modal participation factors for a selected number of modes, as a function of external loading. The actual motion of the tyre/rim in space is finally re-constructed as a linear combination of the eigenfunctions multiplied by their corresponding modal participation factors.

The sliding speed distribution along the length of the tread base is calculated from the belt/rim model as follows:

$$v^{y}_{treadbase}(x) = v^{y}_{rim} + \sum_{n=1}^{N} \dot{q}^{y}_{n} f^{y}_{n}(x) + V_r \frac{\partial}{\partial x} \sum_{n=2}^{N} q^{y}_{n} f^{y}_{n}(x), x \in (-\text{a,a}) \quad (38)$$

$$v^{x}_{treadbase}(x) = v^{x}_{rim} + \dot{x}_b cos\left(\frac{x}{R}\right) + \dot{x}'_b cos\left(\frac{x}{R} - \frac{\pi}{2}\right)$$

$$+ \sum_{n=1}^{N} \dot{q}^{x}_{n} f^{x}_{n}(x) + V_r \frac{\partial}{\partial x} \sum_{n=2}^{N} q^{x}_{n} f^{x}_{n}(x), x \in (-\text{a,a}) \quad (39)$$

In eq. (38), (39), $v^{y,x}_{treadbase}$ is the velocity at the base of the tread $[ms^{-1}]$ in the lateral and longitudinal directions, $v^{y,x}_{rim}$ is the rim velocity $[ms^{-1}]$, $q^{y,x}_{n}$ is the modal participation factor of the n^{th} mode in y, x $[m]$, $f^{x,y}_{n}$ is the corresponding eigenfunction of the n^{th} mode, V_r is the linear speed of rolling $[ms^{-1}]$ and N is the maximum number of modes considered.

The tread-base velocities from eq. (38), (39) are applied at the roots of flexible bristles representing tread compliance. The bristles deflect according to the following law:

$$\delta^{y,x}_{tread}(x) = \begin{cases} \int v^{y,x}_{treadbase}(x)dt, if \left| c^{y,x} \delta^{y,x}_{tread}(x) \right| < f_z(x)\mu(x) \\ \frac{f_z(x)\mu(x)}{c^{y,x}}, if \left| c^{y,x} \delta^{y,x}_{tread}(x) \right| \geq f_z(x)\mu(x) \end{cases} \quad (40)$$

In eq. (40) $\delta^{y,x}_{tread}$ is tread deflection in y, x directions $[m]$, $c^{y,x}$ is the stiffness of the bristles per unit length $[Nm^{-2}]$, $f_z(x)$ is the local load distribution $[Nm^{-1}]$ and $\mu(x)$ is the local coefficient of friction.

The global sliding speed of the bristle tips is finally calculated as:

$$v^{y,x}_{treadtip}(x) = v^{y,x}_{treadbase}(x) + V_r \frac{\partial}{\partial x} \delta^{y,x}_{tread}(x) \quad (41)$$

To demonstrate the response of the structural model, the lateral case is taken forward. The parameters of the structural model were roughly tuned to provide a tyre with cornering stiffness of approx. 45000 $[Nrad^{-1}]$ and a lateral relaxation length of approx. 0.55 m at a vertical load of 6000 $[N]$. The response of the lateral model to a step-steer angle of 0.02 $[rad]$ is shown in fig. 15 and is in good agreement with [16] (see for example p. 482, fig 9.46).

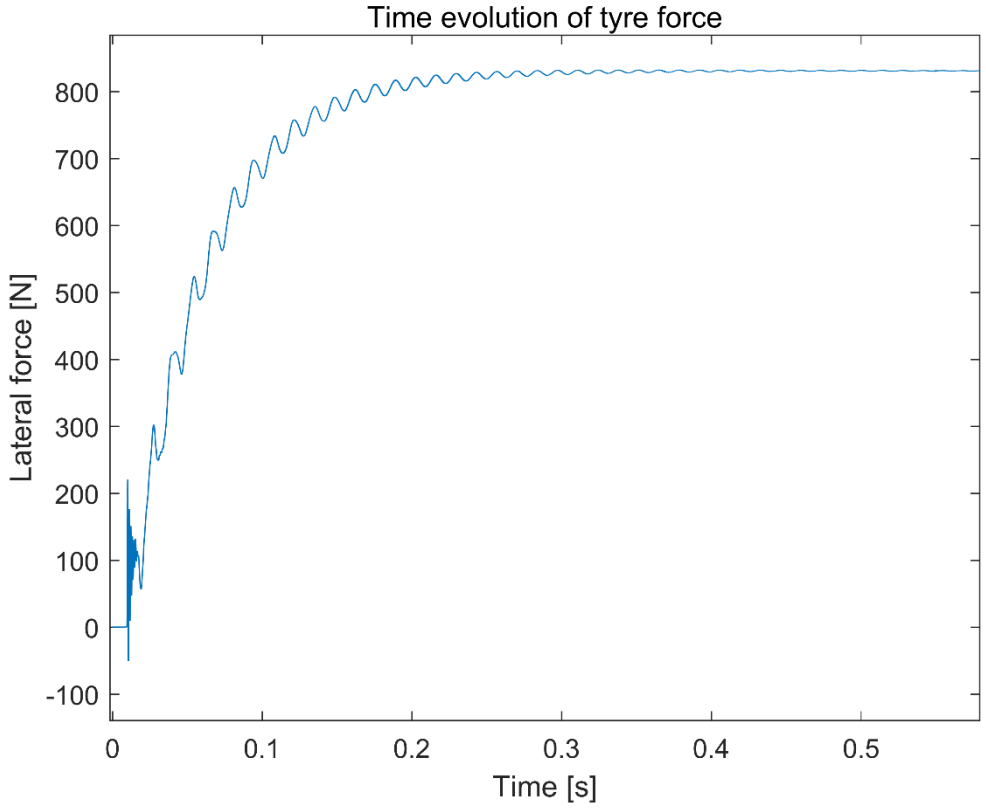

Figure 15. Step response to a lateral slip angle of 0.02 $[rad]$ at a forward speed of 10 $[ms^{-1}]$, under a vertical load of 6000 $[N]$, assuming a constant coefficient of friction $\mu = 1$ along the contact.

Combined model

The macroscopic heat-transfer model is combined with the flash temperature model and the structural model to create a complete tyre model with bulk and flash temperature effects. A truly transient solution at the contact patch requires simultaneous consideration of as many macroscopic contact areas as might exist in the contact. This approach is prohibited on the grounds of computational cost. Instead, a quasi-transient approach is adopted whereby snapshots of the tread are taken at a frequency which is high enough to capture the basic structural dynamics and bulk thermal dynamics. For the lateral relaxation length response presented in the previous section the bandwidth reaches 9 $[Hz]$ at 30 $[ms^{-1}]$ forward speed. The bulk thermal dynamics are similarly slow with an adequate time-step of 0.01 $[s]$ (see table B.1 in Appendix B). As a compromise between accuracy and efficiency tread snapshots are taken at a frequency of 20 $[Hz]$. For every snapshot, it is assumed that belt deformation and its rate, as well as bulk temperature distribution at the tread, all remain constant. The time-history of a single representative macro-asperity contact is then considered from the moment the asperity enters the leading edge of the contact until it exits at the trailing edge. The local normal pressure, sliding speed and bulk temperature are employed – the latter as a boundary condition – as the macro-asperity contact moves to the rear (in fact the tyre rolls over the asperity) and friction is continuously updated including the effect of flash temperature. The local deformation and sliding speed of the tread are calculated using eq. (40) and (41).

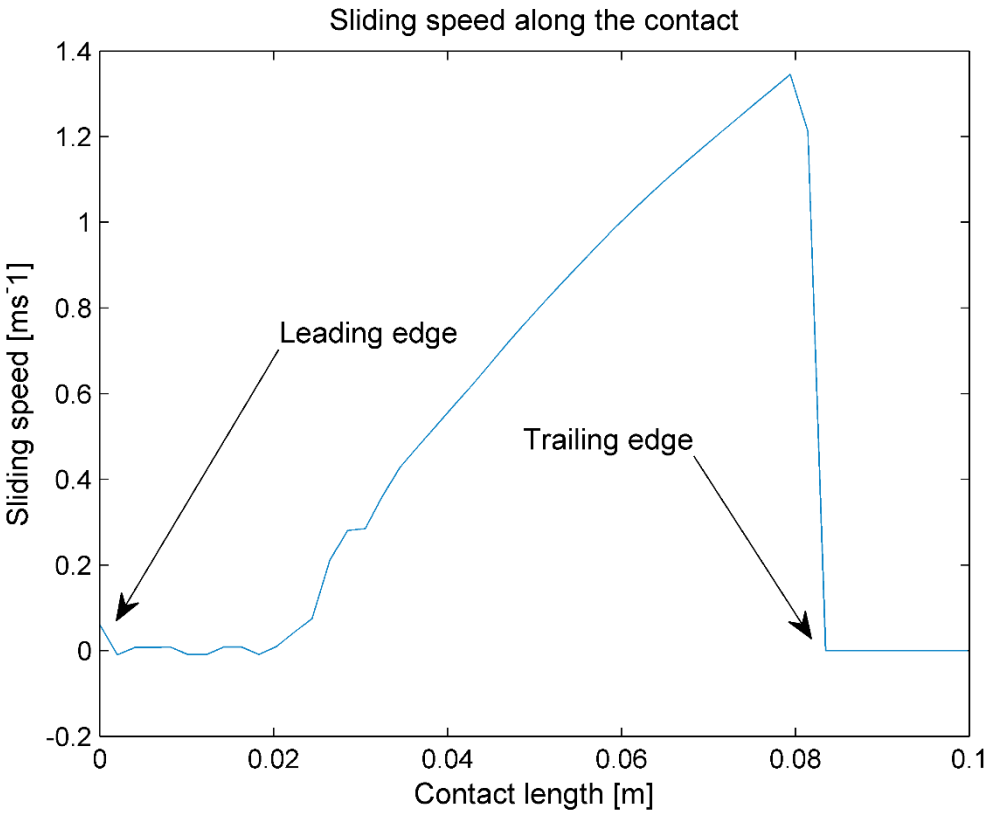

Figure 16. Lateral sliding speed along the contact 0.5 $[s]$ after a step lateral slip input of 0.02 $[rad]$ at a forward speed of 30 $[ms^{-1}]$ and a vertical load of 1500 $[N]$. The initial temperature of the tyre is 27°C.

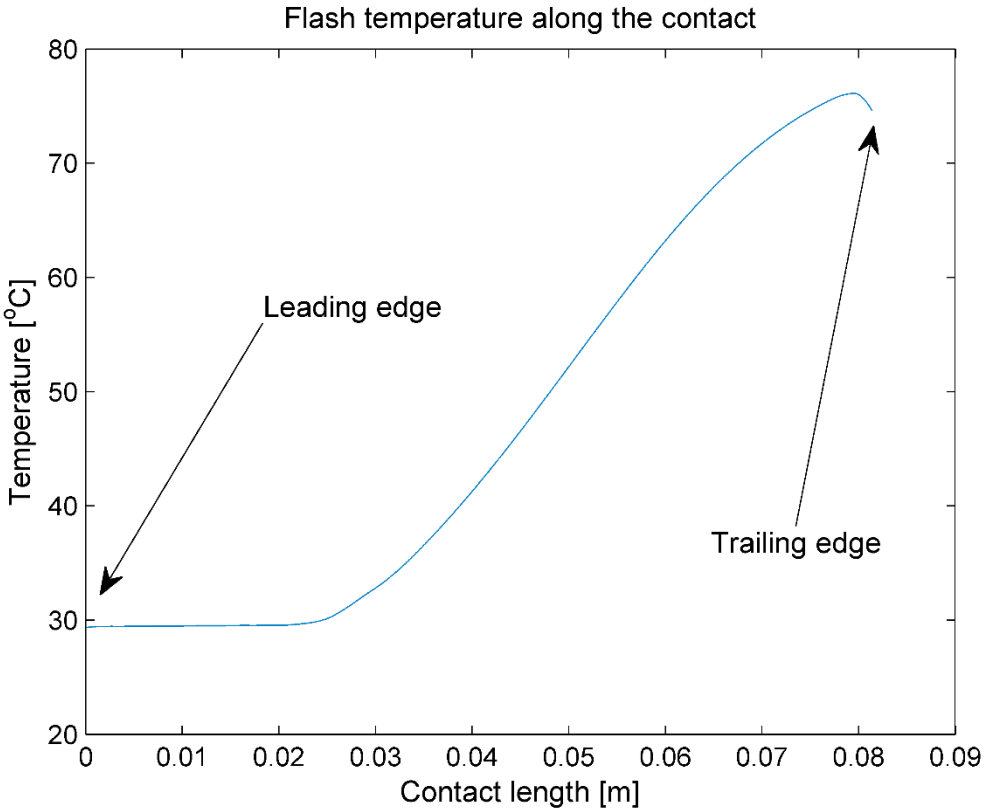

Figure 17. Flash temperature along the contact 0.5 $[s]$ after a step lateral slip input of 0.02 $[rad]$ at a forward speed of 30 $[ms^{-1}]$ and a vertical load of 1500 $[N]$. The initial temperature of the tyre is 27°C.

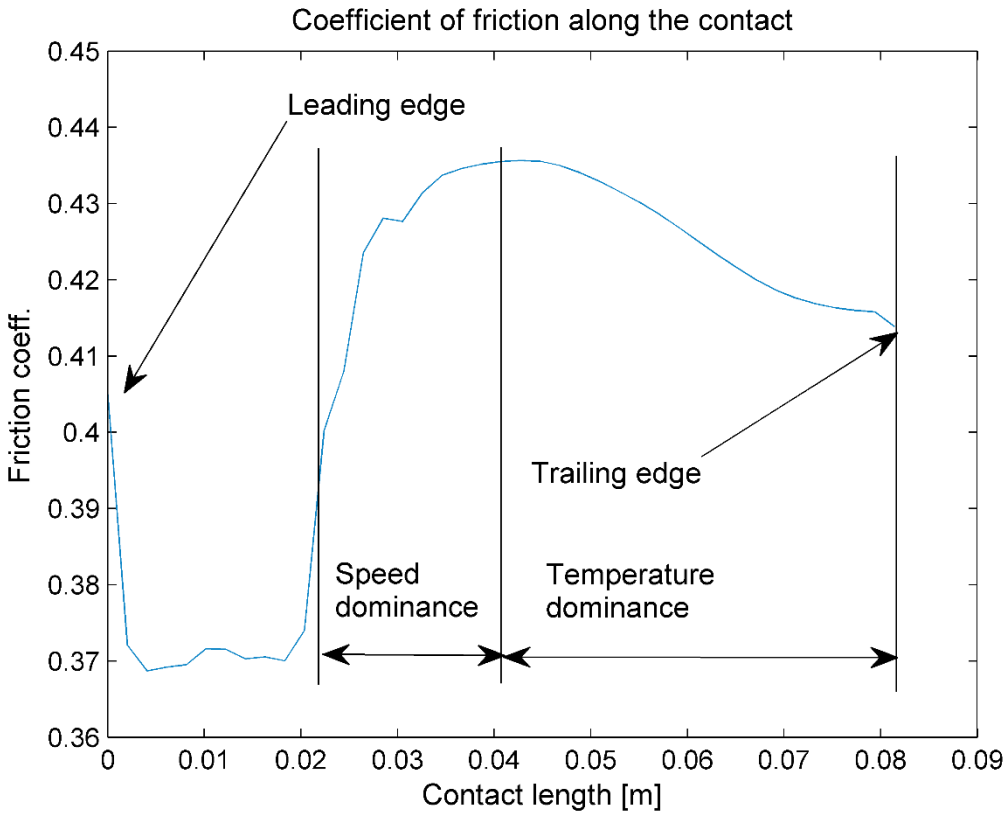

Figure 18. Friction coefficient along the contact 0.5 $[s]$ after a step lateral slip input of 0.02 $[rad]$ at a forward speed of 30 $[ms^{-1}]$ and a vertical load of 1500 $[N]$. The initial temperature of the tyre is 27°C.

Examples of the sliding speed, flash temperature and friction coefficient along the contact are illustrated in figs. 16-18. The results shown refer to a snapshot 0.5 $[s]$ after a step lateral slip input and neglect conduction between the tread and the road. The simulation time for the model to complete a single contact snapshot is approx. 1300 $[s]$ on one core of an Intel® i5 processor.

As shown in fig. 16 the tread enters the contact with a small sliding speed due to rim/belt motion. Friction develops rapidly (see fig. 10 for the expected friction at different speeds/temperatures) and stretches the tread, thereby reducing its sliding speed and with it the expected friction (see fig. 18). The tread then practically sticks to the road with no increase in flash temperature, as shown in fig. 17. Sliding starts when the 2nd likelihood of eq. (40) is valid. The sliding speed increases significantly as shown in fig. 16 and with it the flash temperature builds up rapidly. The friction initially increases due to the sliding speed increasing and reaches a peak after which it reduces as the temperature effect becomes dominant.

Conclusions

A thermo-frictional tyre model has been developed, capable of simulating both macroscopic and flash temperature evolution. The model combines a macroscopic heat-transfer model, a flash temperature model and a structural tyre model.

An alternative formulation of the flash-temperature problem was proposed that accommodates a varying bulk temperature as well as conduction with the road. Simulation results indicate that, if perfect conduction is assumed between the rubber and the road, the predicted flash temperature reduces significantly. It is expected that conduction will be reduced due to non-perfect contact within the macro-asperity contact areas and possibly because of contamination, although the latter could promote conduction, depending on the nature of contamination (e.g. liquid trapped in asperities). In any case, further work is required to quantify conduction between road/rubber.

Using the complete model, simulation results were obtained for the sliding speed, flash temperature and friction along the contact. While the model is computationally intensive, it can be used to establish the frictional envelope of a whole tyre, considering not only the properties of tread rubber but also the influence of structural properties.

Acknowledgments

I would like to thank Jan Prins from Jaguar Land Rover for his continuous support during the validation of the macroscopic heat transfer model. Also, Henning Olson and David Gentz from Calspan and Mateo Gladstone and Greg Smith from JLR for their help with tyre measurements.

References

[1] Grosch, K.A., *The Relation between the Friction and Visco-Elastic Properties of Rubber*, Proceedings of the Royal Society of London. Series A, Mathematical and Physical Sciences, 274:1356 (1963), pp. 21-39.
[2] Williams, M.L., Landel, R.F. and Ferry, J.D., *The Temperature Dependence of Relaxation Mechanisms in Amorphous Polymers and Other Glass-forming Liquids*, Journal of the American Chemical Society, 77:14 (1955), pp. 3701-3707.
[3] Persson, B.N.J., *Theory of rubber friction and contact mechanics*, J. Chem. Phys., 115:8 (2001), pp. 3840-3861.
[4] R. S. Sharp, P. Gruber and E. Fina, *Circuit racing, track texture, temperature and rubber friction*, Vehicle System Dynamics, 54:4 (2016), pp. 510-525.
[5] Persson, B.N.J., *Rubber Friction: role of the flash temperature*, J. Phys.: Condens. Matter, 18 (2006), pp. 7789-7823.
[6] Persson, B.N.J., *Rubber friction and tire dynamics*, J. Phys.: Condens. Matter, 23 (2011), 015003 (14pp).
[7] Mizuno, M., Sakai, H., Oyama, K. and Isomura, Y., *Development of a tyre force model incorporating the influence of the tyre surface temperature*, Vehicle System Dynamics, 43 (2005), pp. 395-402.
[8] Gipser, M., *FTire: A physically based application-oriented tyre model for use with detailed MBS and finite-element suspension models*, Vehicle System Dynamics, 43 (2005), pp. 76-91.
[9] Fevrier, P., *Thermal and Mechanical Tire Force and Moment Model*, IPG Technology Conference, Ettlingen, 2008.
[10] Durand-Gasselin, B., Dailliez, T., Mossner-Beigel, M., Knorr, S., Rauh, J., *Assessing the thermomechanical TaMeTirE model in off-line vehicle simulation and driving simulator tests*, IAVSD symposium, Stockholm, 2009.
[11] Sorniotti, A., *Tire Thermal Model for Enhanced Vehicle Dynamics Simulation*, SAE paper 2009-01-0441.
[12] Calabrese, F., Baecker, M., Galbally, C., and Gallrein, A., *A Detailed Thermo-Mechanical Tire Model for Advanced Handling Applications*, SAE Int. J. Passeng. Cars - Mech. Syst. 8:2 (2015), pp. 501-511.
[13] Juma, M. and Bafrnec, M., *Heat Transfer Properties of Cord-reinforced Rubber Composites*, Journal of Reinforced plastics and composites, 25: 18 (2006), pp. 1967-1975.
[14] Incropera, P. et al., *Fundamentals of heat and mass transfer*, John Willey and Sons, 2007.

[15] Besselink, I. J. M., Schmeitz, A. J. C. and Pacejka, H. B., *An improved Magic Formula/Swift tyre model that can handle inflation pressure changes*, Vehicle System Dynamics, 48: 1 (2010), pp. 337-352.

[16] Pacejka, H. B., *Tyre and Vehicle Dynamics*, Butterworth-Heinemann, 2007.

[17] Fraggstedt, M., *Vibrations, damping and power dissipation in car tyres*, Doctoral Thesis, KTH, Stockholm, 2008.

[18] Thieme, H. van Eldik, Dijks, A.J. and Bobo, S., *Measurement of Tire Properties*, In: Clark, S.K. (editor), Mechanics of Pneumatic Tyres, Washington D.C., 1981.

[19] Popov, A.A., Cole, D.J., Winkler, C.B. and Cebon, D., *Laboratory measurement of rolling resistance in truck tyres under dynamic vertical load*, Proc Inst Mech Eng Part D: Journal of Automobile Engineering, 217 (2003), pp. 1071-1079.

[20] Browne, A.L. and Wickliffe, L.E., *Parametric Study of Convective Heat Transfer Coefficients at the Tire Surface*, Tire Science and Technology, 8:3-4 (1980), pp. 37-67.

[21] Farroni, F., Giordano, D., Russo, M. and Timpone, F., *TRT: thermo racing tyre a physical model to predict the tyre temperature distribution*, Meccanica, 49 (2014), pp. 707-723.

[22] Coleman, T.F. and Li, Y., An Interior, Trust Region Approach to Nonlinear Minimisation Subject to Bounds, SIAM Journal on Optimisation, 6:2 (1996), pp. 418-445.

[23] Whitehouse, D. J. and Archard, J. F., *The properties of random surfaces of significance in their contact*, Proc. Roy. Soc., A316 (1970), pp. 97-121.

[24] Feder, J., *Fractals*, Plenum, 1988.

[25] Isono, Y. and Aoyama, T., *Filler Effects on Temperature Shift Factors in Viscoelastic Properties of Carbon Black Filled Rubbers*, Journal of the Society of Rheology, Japan, 41:3 (2013), pp. 137-144.

[26] Lorenz, B., Persson, B.N.J., Fortunato, G., Giustiniano, M. and Baldoni, F., *Rubber friction for tire tread compound on road surfaces*, J. Phys.: Condens. Matter, 25 (2013), 095007 (8pp).

[27] Tsotras, A. and Mavros, G., *Frictional contact behaviour of the tyre: The effect of tread slip on the in-plane structural deformation and stress field development*, Vehicle System Dynamics, 48:8 (2009), pp. 891-921.

[28] Soedel, W., *Vibrations of Shells and Plates*, Marcel Dekker Inc., New York, 2004.

[29] Gong, S., *A study of in-plane dynamics of tyres*, Doctoral Thesis, Delft University of Technology, The Netherlands, 1993.

[30] Zegelaar, S., *The dynamic response of tyres to brake torque variations and road unevenesses*, Doctoral Thesis, Delft University of Technology, The Netherlands, 1998.

[31] Tsotras, A. and Mavros, G., *The simulation of in-plane tyre modal behaviour: a broad modal range comparison between analytical and discretised modelling approaches*, Vehicle System Dynamics, 47:11 (2009), pp. 1377-1400.

APPENDIX A: A note on road surface temperature

Three case studies were conducted to illustrate the occasions when solution of the road heat-transfer equation (2) can be omitted and tread-road conduction can be treated using a constant road temperature. The results of all three case studies are shown in fig. A.1. In all cases, a tyre with dimensions and properties as defined in Appendix B is loaded with 5000 N vertically, driven at a forward speed of 10 ms^{-1}, with tractive slip ratio of 0.5, on an asphalt road of 300 mm depth. A snapshot of the road temperature distribution along the direction of travel is taken 30 seconds after the start of each simulation. In the first case (fig. A.1 (a)), the road is held artificially stationary with respect to the contact patch (i.e. the same road block follows the tyre as it moves forward). Because the hot contact patch is always in contact with the same part of the road, there is a significant rise of 20^{o}C in the surface temperature of the road. The second case (fig. A.1 (b)) simulates the situation where the road surface circulates periodically, as is the case on drum or flat-track tyre test rigs. The

length of the road is 3 metres. The temperature rise is now reduced to approximately 2°C. This is due to the contact interacting with a much larger volume of road and the associated convective cooling of this volume when not in contact with the tread. Finally, the case where the tyre advances forward normally (or, equivalently, the road moves rearwards) is shown in fig. A.1 (c). The temperature rise after 30 *s* is now only 0.4°C. Clearly, in case (c) and potentially case (b), the temperature of the road can be assumed constant. It must be noted that after prolonged testing periods on flat-track machines the surface temperature is likely to increase significantly due to the low diffusivity of the abrasive papers used on such machines. This effect was included in the validation simulations of the heat-transfer model by using equation (7) with the track surface temperature that was acquired during all measurements at Calspan.

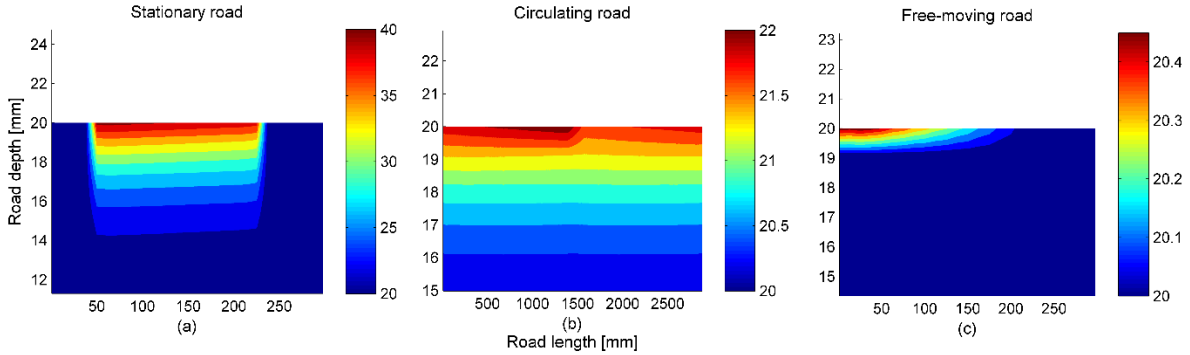

Figure A.1. Three extremes of road heating: In (a) the road is stationary with respect to the tyre and its surface temperature rises significantly. In (b) the contact between tread/road recurs periodically and in (c) the road moves with respect to the contact as dictated by the forward speed of the tyre.

APPENDIX B: Parameters used in macroscopic heat-transfer model

Parameter	Units	Value	Source	Comments
Dimensions				
Outer radius	[m]	0.395	Measured	
Rim radius	[m]	0.254	Measured	
Tread width	[m]	0.225	Measured	
Tread thickness	[m]	0.018	Measured	
Sidewall nominal thickness	[m]	0.004	Measured	
Material				
Material average density	[kgm^{-3}]	1.10E+03	Nominal [13]	
Reinforced rubber specific heat	[$Jkg^{-1}K^{-1}$]	1765.5	***Identified***	Good agr. with [13]
Radial tread conductivity	[$Wm^{-1}K^{-1}$]	3.01E-01	***Identified***	Good agr. with [13]
Angular tread conductivity	[$Wm^{-1}K^{-1}$]	3.03E-01	Nominal [13]	
Transverse tread conductivity	[$Wm^{-1}K^{-1}$]	3.03E-01	Nominal [13]	
Radial sidewall conductivity	[$Wm^{-1}K^{-1}$]	3.03E-01	Nominal [13]	
Angular sidewall conductivity	[$Wm^{-1}K^{-1}$]	3.03E-01	Nominal [13]	
Transverse sidewall conductivity	[$Wm^{-1}K^{-1}$]	2.15E-01	Nominal [13]	
Inflation air specific heat	[$Jkg^{-1}K^{-1}$]	7.23E+02	Nominal	
Heat distribution				
Roll. res. coeff. rr_a	[sm^{-1}]	2.79E-04	***Identified***	

Roll. res. coeff. rr_b	[s^2m^{-2}]	2.00E-06	***Identified***	
Lat. ref. load $F_{y,ref}$ *(eq. 12)*	[N]	7.21E+03	***Identified***	
Long. ref. load $F_{x,ref}$ *(eq. 11)*	[N]	8.52E+03	***Identified***	
B_y *(eq. 12)*	Dimensionless	0.023	***Identified***	
B_x *(eq. 11)*	Dimensionless	0.001	***Identified***	
Reference camber γ_{ref} *(eq.15)*	[degrees]	2.9	***Identified***	
Heating depth, H_T	[m]	0.010	***Identified***	
Heat exchange				
External convection param. h_a	[$WK^{-1}m^{-2}$]	5.00E+00	***Identified***	Good agr. with [20]
External convection param. h_b	[$WK^{-1}m^{-3}s$]	7.00E+00	***Identified***	Good agr. with [20]
Internal convection coefficient	[$WK^{-1}m^{-2}$]	8.00E+01	***Identified***	Good agr. with [20]
Rubber emissivity	Dimensionless	0.94	Nominal	
Simulation				
Radial tread elements		50	***Identified***	
Transverse tread elements		2		
Angular tread elements		200		
Radial sidewall elements		2		
Transverse sidewall elements		1		
Angular sidewall elements		1		
Time-step	[s]	1.00E-02		
Environment				
Mean ambient temperature	[^oC]	27	Measured	
Road conductivity	[$Wm^{-1}K^{-1}$]	7.50E-01	Nominal	

Table B.1: Macroscopic heat-transfer model parameters

APPENDIX C: Parameters used in flash temperature model

Parameter	Units	Value	Source
Dimensions			
Macro-asperity contact radius	[m]	0.001	Calculated (eq. 23)
Material			
Material average density	[kgm^{-3}]	1.10E+03	Nominal [13]
Rubber specific heat	[$Jkg^{-1}K^{-1}$]	1560	Nominal [13]
Rubber conductivity	[$Wm^{-1}K^{-1}$]	3.03E-01	Nominal [13]
Simulation			
Mesh size in z-direction	[μm]	2	
Mesh size in radial direction	[μm]	250	
No of angular mesh elements		12	
Timestep	[s]	2.27E-06	
Environment			
Starting rubber temperature	[^oC]	27	Nominal

Road average density	[kgm^{-3}]	2.36E+03	Nominal
Road conductivity	[Wm^{-1}K^{-1}]	7.50E-01	Nominal
Road specific heat	[Jkg^{-1}K^{-1}]	9.20E+02	Nominal

Table C.1: Flash temperature model parameters

APPENDIX D: Solution of structural equations

D.1 Equations for lateral motion

Solution of eq. (28)-(31) is achieved by modal expansion. The following sets of solutions are considered:

$$v_1(x,t) = Be^{i\omega_n t}\cos\left(n\frac{x}{R}\right), for\ n = 0,1,\dots,\infty \text{ (D.1)}$$

$$v_2(x,t) = Be^{i\omega_n t}\cos\left(n\frac{x}{R}-\frac{\pi}{2}\right), for\ n = 0,1,\dots,\infty \text{ (D.2)}$$

$$y(t) = Ce^{i\omega_n t}, for\ n = 0 \text{ (D.3)}$$

$$\varphi(t) = De^{i\omega_n t}, for\ n = 1 \text{ (D.4)}$$

$$\psi(t) = De^{i\omega_n t}, for\ n = 1 \text{ (D.5)}$$

Solutions $v_{1,2}$ are orthogonal to each-other for $n > 0$ and allow deflection in all possible directions. Note that solutions $v_{1,2}$ for $n = 0$ are identical and are the only solutions that couple equations (28) and (29). Accordingly, the coupling term $-k_y y_{\omega_0}$ vanishes from eq. (28) for all frequencies other than ω_0. This is indicated by the subscript ω_0 in degree of freedom y in eq. (28) and (29). Degrees of freedom φ and ψ represent orthogonal rotations of the wheel rim about axes x (camber) and z (yaw), respectively. From eq. (30) degree of freedom φ interacts with v_1 for $n = 1$ only, otherwise the term $-k_y\varphi_{\omega_1}Rcos\left(\frac{x}{R}\right)$ from eq. (28) vanishes. This is indicated by the subscript ω_1 in degree of freedom φ in eq. (28) and (30). Similar observations apply to degree of freedom, ψ.

Solution of lateral tyre deflection involves calculation of a subset of eigenvalues, say from $n = 0,\dots,N$ and the associated eigenfunctions. The cases where $n = 0$ and $n = 1$ are considered separately in eigenvalue calculation as detailed below.

For $n = 0$ we substitute solutions (D.1) and (D.3) into eq. (28) and (29) to obtain:

$$\begin{bmatrix} -\rho A\omega_0^2 + k_y & -k_y \\ -k_y & -\frac{m_w}{2\pi R}\omega_0^2 + k_y \end{bmatrix}\begin{bmatrix} B \\ C \end{bmatrix} = \begin{bmatrix} 0 \\ 0 \end{bmatrix} \text{ (D.6)}$$

Solving the system's characteristic polynomial yields two eigenvalue pairs, ω_0:

$$\omega_{0,1} = \pm 0 \text{ (D.7)}$$

$$\omega_{0,2} = \pm\sqrt{\frac{k_y(\rho A+\frac{m_w}{2\pi R})}{\rho A\frac{m_w}{2\pi R}}} \text{ (D.8)}$$

The first pair corresponds to the rigid body mode whereby the rim moves laterally with the tyre without relative deflection. The second solution-pair corresponds to the out-of-phase lateral motion of the tyre-rim assembly. Substituting the eigenvalues (D.7) and (D.8) back into eq. (D.6) gives the eigenfunction amplitudes B and C as follows:

$$B = C, for\ \omega_{0,1} \text{ (D.9)}$$

$$\frac{B}{C} = -\frac{m_w}{2\pi R\rho A}, for\ \omega_{0,2} \text{ (D.10)}$$

The eigenfunctions are mass-normalised by requesting that:

$$B^2(2\pi R\rho A + m_w) = 1, for\ \omega_{0,1} \text{ (D.11)}$$

$$B^2(2\pi R\rho A + (2\pi R\rho A)^2/m_w) = 1, for\ \omega_{0,2} \text{ (D.12)}$$

For $n = 1$ we substitute solutions (D.1) and (D.4) into eq. (28) and (30). It is worth observing that due to coincidence of the start and end of the tyre belt and the resulting symmetry about the spin-axis, the mode $n = 1$ does not involve flexing of the belt. Observing the displaced tyre belt with $n = 1$ from the side and assuming amplitude of deflection, B, and radius of belt, R, it is possible to obtain the slope of the displaced belt as follows:

$$\frac{\partial v}{\partial \xi} = \frac{(B - Bcos\left(\frac{x}{R}\right))}{(R - Rcos\left(\frac{x}{R}\right))} = \frac{B}{R} = const \text{ (D.13)}$$

where ξ is the projection of the circular belt on the observation plane.

Clearly, in that case the belt lies in a single plane so that both spatial derivative terms in eq. (28) vanish. With this observation, we obtain:

$$\begin{bmatrix} -\rho A\omega_1^2 + k_y & -k_y R \\ -k_y R & -\frac{Ixx_w}{\pi R}\omega_1^2 + k_y R^2 \end{bmatrix} \begin{bmatrix} B \\ D \end{bmatrix} = \begin{bmatrix} 0 \\ 0 \end{bmatrix} \text{ (D.14)}$$

Solving the system's characteristic polynomial yields two eigenvalue pairs, ω_1:

$$\omega_{1,1} = \pm 0 \text{ (D.15)}$$

$$\omega_{1,2} = \pm \sqrt{\frac{k_y(R^2\rho A + \frac{Ixx_w}{\pi R})}{\rho A \frac{Ixx_w}{\pi R}}} \text{ (D.16)}$$

It is worth noting that the omission of spatial derivatives for $n = 1$ is further justified by the existence of a rigid mode, as demonstrated by eq. (D.15).

Substituting the eigenvalues (D.15) and (D,16) back into eq. (D.14) gives the eigenfunction amplitudes B and D as follows:

$$\frac{B}{D} = R, for\ \omega_{1,1} \text{ (D.17)}$$

$$\frac{B}{D} = -\frac{Ixx_w}{\pi R^2 \rho A}, for\ \omega_{1,2} \text{ (D.18)}$$

The eigenfunctions are mass-normalised by requesting that:

$$B^2(\rho A\pi R + Ixx_w/R^2) = 1, for\ \omega_{1,1} \text{ (D.19)}$$

$$B^2(\rho A\pi R + (\pi R^2\rho A)^2/Ixx_w) = 1, for\ \omega_{1,2} \text{ (D.20)}$$

The amplitudes and eigenvalues calculated above for the set of solutions $v_1(x,t)$, $\varphi(t)$ and $n = 1$ are identical to those obtained for the set of solutions $v_2(x,t)$, $\psi(t)$ and $n = 1$. Both orthogonal sets are however retained to account for deflection of arbitrary orientation.

Finally, we deal with the case $n > 1$ which includes all flexible modes of the belt. The eigenvalues are easily obtained as:

$$\omega_{(n>1),1\&2} = \pm\sqrt{\frac{n^4 EI}{\rho A R^4} + \frac{n^2 P_0 b}{\rho A R} + \frac{k_y}{\rho A}} \text{ (D.21)}$$

Accordingly, the amplitude that mass-normalises the eigenfunctions is given by:

$$B^2(\rho A \pi R) = 1, for\ \omega_{n>1} \text{ (D.22)}$$

D.2 Equations for tangential/rotational motion

The following sets of solutions are considered for eq. (32) and (33):

$$u_1(x,t) = Ee^{i\omega_n t}\cos\left(n\frac{x}{R}\right), for\ n = 0,1,\dots,\infty \text{ (D.23)}$$

$$u_2(x,t) = Ee^{i\omega_n t}\cos\left(n\frac{x}{R} - \frac{\pi}{2}\right), for\ n = 0,1,\dots,\infty \text{ (D.24)}$$

$$\theta(t) = Fe^{i\omega_n t}, for\ n = 0 \text{ (D.25)}$$

For $n = 0$ we substitute solutions (D.23) and (D.25) into eq. (32) and (33) to obtain:

$$\begin{bmatrix} -\rho A\omega_0^2 + k_x & -Rk_x \\ -Rk_x & -\frac{Iyy_w}{2\pi R}\omega_0^2 + R^2 k_x \end{bmatrix}\begin{bmatrix} E \\ F \end{bmatrix} = \begin{bmatrix} 0 \\ 0 \end{bmatrix} \text{ (D.26)}$$

The characteristic polynomial yields two eigenvalue pairs, ω_0:

$$\omega_{0,1} = \pm 0 \text{ (D.27)}$$

$$\omega_{0,2} = \pm\sqrt{\frac{k_x(\rho AR^2 + \frac{Iyy_w}{2\pi R})}{\rho A\frac{Iyy_w}{2\pi R}}} \text{ (D.28)}$$

The first solution-pair corresponds to the rigid body rotational motion of the rim-tyre around the spin-axis, y, while the second solution-pair corresponds to the out-of-phase rotational motion of the belt with respect to the rim.

Substitution of the eigenvalues (D.27) and (D.28) into (D.26) gives the eigenfunction amplitudes, E and F:

$$\frac{E}{F} = R, for\ \omega_{0,1} \text{ (D.29)}$$

$$\frac{E}{F} = -\frac{Iyy_w}{2\pi R^2 \rho A}, for\ \omega_{0,2} \text{ (D.30)}$$

The eigenfunctions are mass-normalised by requesting that:

$$E^2\left(2\pi R\rho A + \frac{Iyy_w}{R^2}\right) = 1, for\ \omega_{0,1} \text{ (D.31)}$$

$$E^2(2\pi R\rho A + (2\pi R^2\rho A)^2/Iyy_w) = 1, for\ \omega_{0,2} \text{ (D.32)}$$

For $n > 0$ we substitute solutions (D.23) into eq. (32) to obtain:

$$\omega_{(n>0),1\&2} = \pm\sqrt{\frac{n^2 E}{\rho R^2} + \frac{k_x}{\rho A}} \text{ (D.33)}$$

Accordingly, the amplitude of the mass-normalised eigenfunctions is given by:

$$E^2(\rho A \pi R) = 1, for\ \omega_{n>0} \text{ (D.34)}$$

D.3 Equations for relative radial motion of belt with respect to rim

Substituting solutions $z_b = Ge^{i\omega t}$ and $z_w = He^{i\omega t}$ into eq. (34) and (35), the eigenvalue pairs are found equal to:

$$\omega_1 = \pm 0 \text{ (D.35)}$$

$$\omega_2 = \pm\sqrt{\frac{k_r \pi R}{m_w} + \frac{k_r}{2\rho A}} \text{ (D.36)}$$

The first pair corresponds to the rigid in-plane motion of the tyre-rim assembly, while the second corresponds to the out-of-phase in-plane motion of the belt relative to the rim. The associated amplitudes are:

$$G = H, for\ \omega_1 \text{ (D.37)}$$

$$\frac{G}{H} = -\frac{m_w}{2\pi R \rho A}, for\ \omega_2 \text{ (D.38)}$$

The amplitude of the mass-normalised 2×1 eigenvectors is given by:

$$G^2(\rho A 2\pi R + m_w) = 1, for\ \omega_1 \text{ (D.39)}$$

$$G^2(\rho A 2\pi R + (\rho A 2\pi R)^2/m_w) = 1, for\ \omega_2 \text{ (D.40)}$$